University of Crete, Department of Physics

IESL-FORTH

Laser Spectroscopy Laboratories

Master Thesis

“Chiral sensing of gases by signal reversing cavity ringdown polarimetry”

Name: Konstantinos Tazes

Supervisor: Prof. T. Peter Rakitzis

Heraklion 2022

Contents

List of Figures

Abstract

The subject of this thesis, is the presentation of the development of a commercial grade polarimeter which promises unparalleled accuracy, compared to the ones available in market. We present the experimental setup and the results of measurement of chiral optical rotation in gases.

Chiral rotations emerge from the chiral nature of the molecules that make up the samples we aim to measure. Being able to accurately determine chiral rotations is of great importance in multiple scientific fields such as Physics, Chemistry, Pharmacology and Medicine.

In the field of Physics, chiral effects can occur due to the weak-interaction which violates parity. Moving up, optical activity can emerge due to the chiral structure of most molecules that consist of more than a few atoms. Thus measuring chiral rotation can help us determine or verify the values of various fundamental and molecular constants.

In the field of Chemistry and Pharmacology, chiral measurements can help in evaluating enantiomeric excess in mixes. This is particularly important in Pharmacology, where the presence of an unwanted enantiomer can render medicines toxic, as in the historic example of Thalidomide.

In medicine, measuring the concentration of certain chiral substances in samples such as tears, can help with diagnosing multiple conditions such as dry eye.

Our polarimeter is based on enhancing optical rotation via cavity techniques. It is an improved form of Cavity Ringdown Polarimetry refined with birefringence and noise quenching techniques, in the form of counter-propagating beams and signal reversal.

This experimental setup is viable form miniaturization in order to better fit trade standards.

Chapter 1: Theory

1.1 Gaussian beams

In order to determine the spacio-temporal distribution of the light emitted by a laser, we must solve Maxwell's equations under certain conditions. If we assume propagation in the z-direction, we can guess the form of the electric field **E.** This should consist of a slowly varying envelope, multiplied by a phase factor. Thus, we can assume that:

$$E(x,y,z) = E_0\psi(x,y,z)e^{-i(kz-\omega t)} \quad (1.1.1)$$

We must then plug this formula into the wave equation for electric fields:

$$\nabla^2\boldsymbol{E} - \frac{1}{c^2}\frac{\partial^2\boldsymbol{E}}{\partial t^2} = 0 \quad (1.1.2)$$

By assuming that the envelope is slowly varying in regard to the phase factor we can omit the second derivative of z and thus, get the following equation.

$$\frac{\partial^2\psi}{\partial x^2} + \frac{\partial^2\psi}{\partial y^2} - i2k\frac{\partial\psi}{\partial z} = 0 \quad (1.1.3)$$

By solving this equation, we get **E.** Getting the magnetic field **B** is becomes trivial by using the fact that:

$$\boldsymbol{\nabla x B} = -\frac{\partial\boldsymbol{E}}{\partial t} \quad (1.1.4)$$

Solving the aforementioned equations simultaneously we get the so-called Gaussian TEM modes, which are given by the following formula:

$$TEM_{m,p}(\boldsymbol{r},t) = E_{m,p}H_m\left(\frac{\sqrt{2}x}{w(z)}\right)H_p\left(\frac{\sqrt{2}y}{w(z)}\right)\frac{w_0}{w(z)}e^{-\frac{x^2+y^2}{w^2(z)}}e^{-i\left[kz-(1+m+p)tan^{-1}\left(\frac{z}{z_0}\right)\right]}e^{-i\frac{kr^2}{2R(z)}} \quad (1.1.5)$$

Where H_i are the Hermite polynomials of order i, w_0 is known as the beam waist and represents the beam diameter at the focus, $w(z)$ is the beam diameter at any point on the axis of propagations and R(z) is the beam curvature. Finally z_0 is a constant called the Rayleigh length, which roughly represents the distance from the focus, over which the beam diameter remains close to the minimum. The formulas for the aforementioned quantities are the following:

$$z_0 = \frac{\pi w_0^2}{\lambda} \quad (1.1.6)$$

$$R(z) = z\left[1 + \left(\frac{z_0}{z}\right)^2\right] \quad (1.1.7)$$

$$w(z) = w_0\sqrt{1 + \left(\frac{z}{z_0}\right)^2} \quad (1.1.8)$$

In order to get a feeling for what these quantities really mean, we can refer to Figure 1 which displays the propagation of Gaussian beam in space.

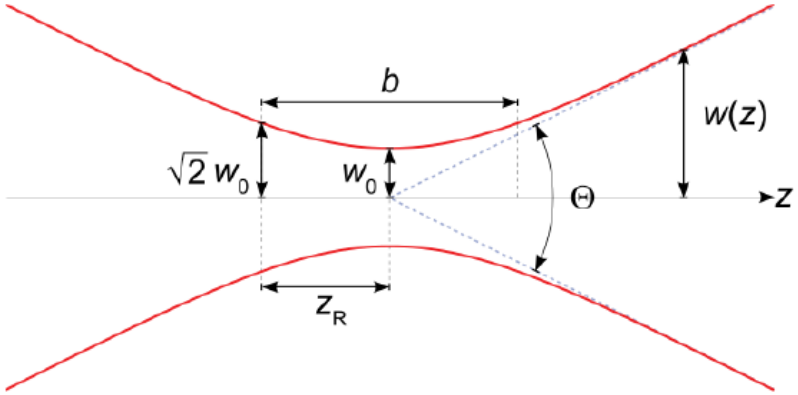

Figure 1: Propagation of a Gaussian beam

Furthermore, in Figure 2 we display the cross sections of the first few TE$M_{m,p}$ modes.

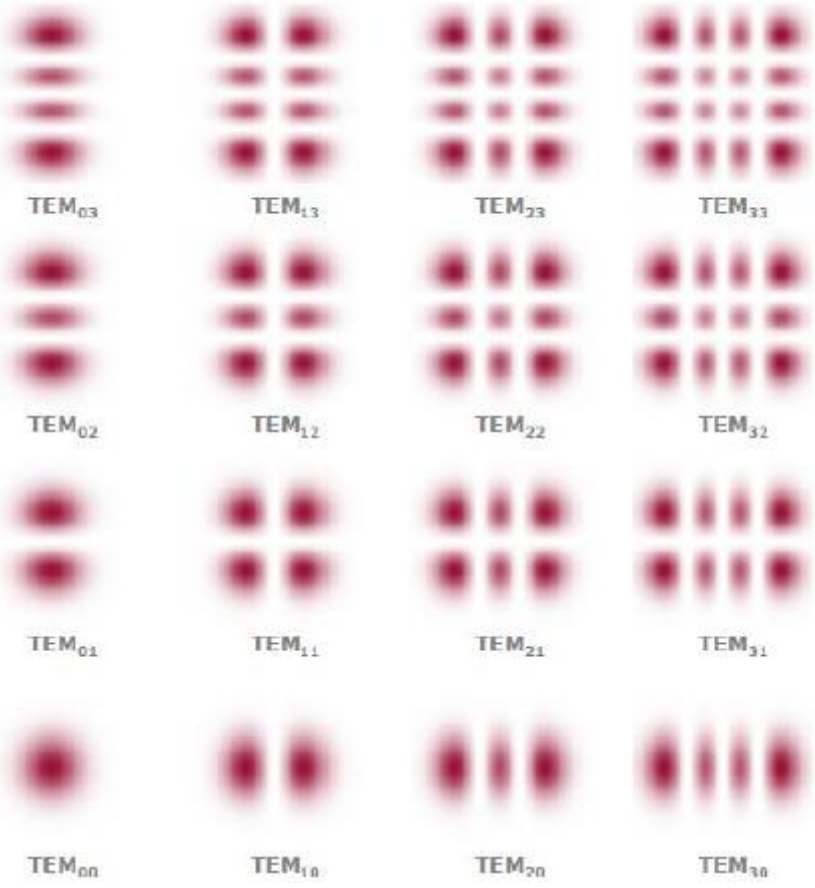

Figure 2: Cross section of TEM modes

1.2 Jones Calculus

In order to study the polarization of light, we must develop the proper tools which will significantly simplify the problem of polarization manipulation and make the expressions much less cumberstone. To this end, we employ Jones calculus. We denote the electric field as such:

$$\boldsymbol{E} = \begin{pmatrix} E_x(t) \\ E_y(t) \end{pmatrix} = \begin{pmatrix} E_{0x} e^{-i(kz-\omega t-\varphi_x)} \\ E_{0y} e^{-i(kz-\omega t-\varphi_y)} \end{pmatrix} \sim \begin{pmatrix} E_{0x} e^{i\varphi_x} \\ E_{0y} e^{i\varphi_y} \end{pmatrix} \quad (1.2.1)$$

We can categorize light into three main categories based on the polarization:

$$\text{Linear: } \boldsymbol{E}_{lin} = \begin{pmatrix} a \\ b \end{pmatrix} \quad (1.2.2)$$

$$\text{Circular: } \boldsymbol{E}_{cir} = \frac{1}{\sqrt{2}} \begin{pmatrix} 1 \\ \pm i \end{pmatrix} \quad (1.2.2)$$

$$\text{Elliptical: } \boldsymbol{E}_{ell} = \begin{pmatrix} a \\ be^{i\varphi} \end{pmatrix} \quad (1.2.3)$$

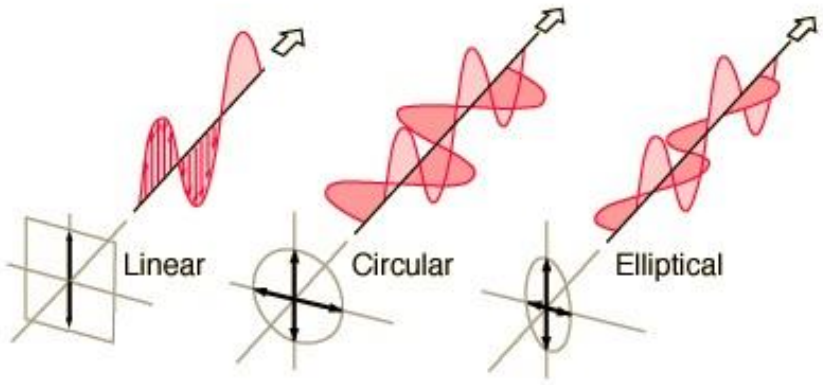

Figure 3: Types of polarization from Laser Teaching Center, Stony Brook University

Each optical element that augments the polarization of light can be described by a 2x2 matrix. The matrices for the elements most commonly used are the following:

Linear polarizer with axis of transmission at angle θ :

$$\begin{pmatrix} cos^2\theta & cos\theta\, sin\theta \\ cos\theta\, sin\theta & sin^2\theta \end{pmatrix} \quad (1.2.5)$$

Half wave plate (HWP) with FA at angle θ:

$$e^{-i\pi/2} \begin{pmatrix} cos^2\theta - sin^2\theta & 2cos\theta\, sin\theta \\ 2cos\theta\, sin\theta & sin^2\theta - cos^2\theta \end{pmatrix} \quad (1.2.6)$$

Quarter wave plate (QWP) with FA at angle θ:

$$e^{-i\pi/4}\begin{pmatrix} cos^2\theta + isin^2\theta & (1-i)cos\theta\ sin\theta \\ (1-i)cos\theta\ sin\theta & sin^2\theta + icos^2\theta \end{pmatrix} \textit{(1.2.7)}$$

Rotation of polarization:

$$\begin{pmatrix} cos\theta & sin\theta \\ -sin\theta & sin\theta \end{pmatrix} \quad \textit{(1.2.8)}$$

Using the above matrices, we can determine the effect, of any assortment of optical elements, on the polarization of light. It is as simple, as multiplying the initial field vector by the matrices corresponding to optical elements. The result will be the final field vector.

We must take into account, the fact that we always measure the integrated intensity over the surface of our photodetection system (A_p) and never the field itself. Thus the signal S is given by:

$$S = \iint_{A_p} I\ dA = \iint_{A_p} \frac{E^+E}{2\eta}\ dA \quad \textit{(1.2.9)}$$

Where η is the impedance of free space η=367.73Ω and "+" denotes the operation of Hermitian conjugation.

One final comment that must be made, is the fact that, Jones calculus applies only to fully polarized light. In the case of partially polarized, we must employ the more complex Mueller calculus which uses 4x4 matrices. In our case, we deal with light which is very close to being 100% polarized, and thus stick to Jones calculus.

1.3 Optical Cavities

An optical cavity is an arrangement of mirrors, within which, the light waves repeat the same path multiple times. We employ high reflectivity mirrors in order to maximize the number of round trips and to simultaneously have a small leakage of light per round trip which will be detected via a photodetector. There are plenty of potential setups for such a cavity. We can split these setups into two categories, running and standing cavities. In a standing cavity , the light is reflected in such a way, that it traverses each point of the cavity twice per round trip. In a running cavity the light always changes direction after each reflection in such a way, that it traverses each point only once per round trip. In order to make this more clear we can refer to Figure 3.

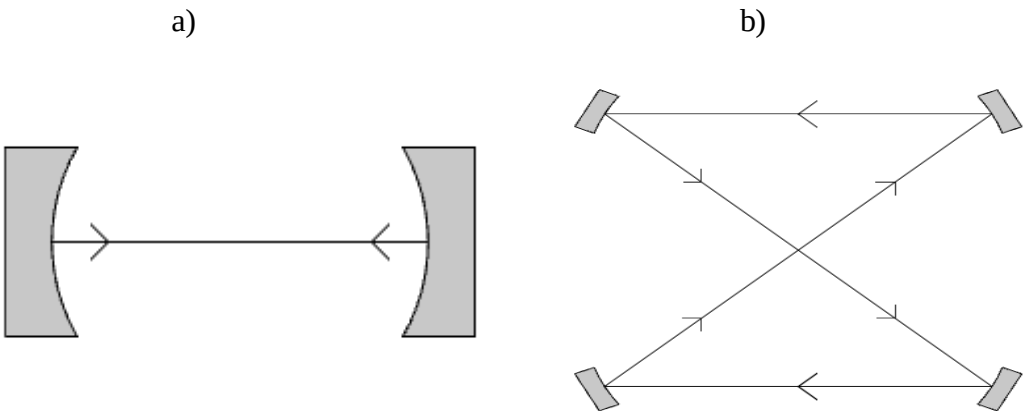

Figure 4: a)Two mirror standing cavity, b)Bow-tie running cavity

The need for optical cavities emerged historically, when people attempted to measure the absorption of light, from samples with very low absorbance. When we attempt to measure such low absorptions through conventional single pass methods, the change in signal amplitude can be so insignificant that it's undetectable by a photodetector. We shall now demonstrate how, a cavity can bring forth a solution to this problem.

Suppose we have a four-mirror bowtie cavity with the mirror reflectivities being R_1, R_2, R_3 and R_4. Furthermore, suppose the light enters the cavity through the mirror M_1 and that we have set a photodetection system after the mirror M_4, with the corresponding reflectivities. If we fire a pulse at the cavity, we will end up with a pulse of initial intensity I_0 inside the cavity. At each mirror, there is a leakage of light, due to the reflectivity not being unity. At then n^{th} round trip, the light inside the cavity, will be:

$$I_n = (R_1R_2R_3R_4)^n I_0 = S^n I_0 = SI_{n-1} \quad (1.3.1)$$

Next up we define, τ_{rt} as the time, that the pulse needs to make a round trip in the cavity. The cavities we work with, have typical lengths of a couple of meters, making τ_{rt} ~ ns. The above formula is discrete, but we can make it continuous by substituting n with $n = \frac{t}{\tau_{rt}}$.

Thus, we get:

$$I(t) = SI(t - \tau_{rt}) \quad (1.3.2)$$

Which can then be Taylor expanded intro:

$$\frac{dI}{dt} = -\frac{1-S}{\tau_{rt}} I = -\frac{1}{\tau_{RD}} I \quad (1.3.3)$$

The solution of this differential equation is simply a decaying exponential.

$$I(t) = I_0 e^{-\frac{t}{\tau_{RD}}} \quad (1.3.4)$$

The light escaping the cavity through M_4 is I(t) multiplied by the corresponding transmissivity T_4

We have also defined the key quantity τ_{RD}, which will be called ringdown time. If we now add a sample into the cavity, of absorbance α, then equations 3.1 and 3.3 become:

$$I_n = (R_1R_2R_3R_4a)^n I_0 = S'^n I_0 = S' I_{n-1} \quad (1.3.5)$$

$$\frac{dI}{dt} = -\frac{1-S'}{\tau_{rt}} I = -\frac{1}{\tau'_{RD}} I \quad (1.3.6)$$

As we can see, a difference in absorbance, leads to different ringdown times, the differences of which are much easier to measure. We can finally determine the absorbance α as:

$$a = \frac{1-\tau_{rt}/\tau'_{RD}}{1-\tau_{rt}/\tau_{RD}} \quad (1.3.7)$$

In figure 4 we show two such signals:

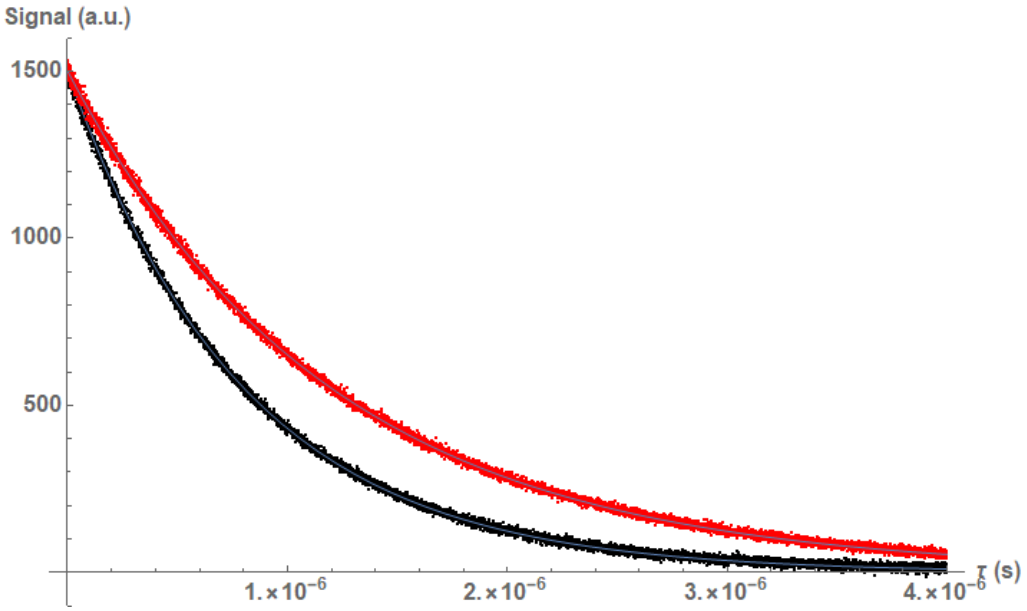

Figure 5: Two ringdown signals with different ringdown times

In our case, the samples not only absorb light, but also rotate its polarization by angle φ per pass. In order to observe the polarization rotation, we place a linear polarizer between M_4 and the photodetector. Thus the light intensity reaching the photodetector becomes:

$$I(t) = T_4 I_0 e^{-t/\tau_{RD}} \cos^2\left(\varphi \frac{t}{\tau_{rt}}\right) = T_4 I_0 e^{-t/\tau_{RD}} cos^2(\omega t) \quad (1.3.8)$$

Signals of this form are displayed in Figure 5

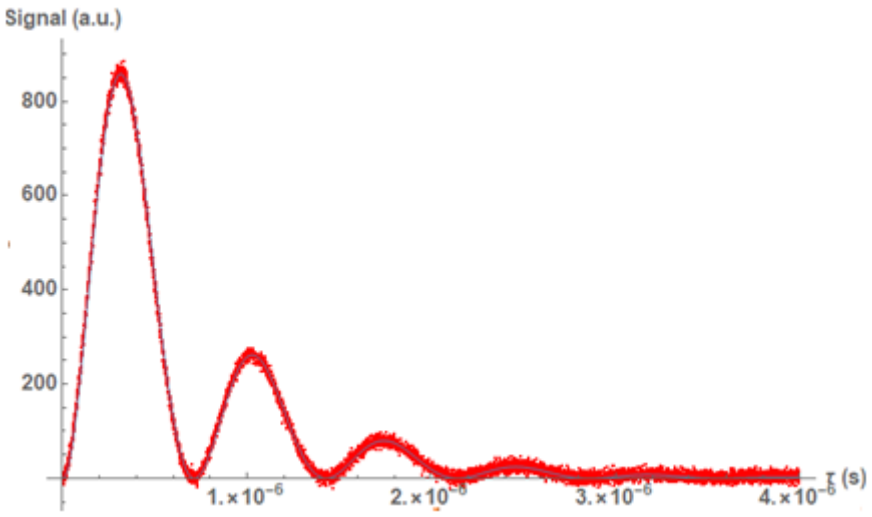

Figure 6: Rigndown signal with optical rotation

In order to determine the optical rotation, we must deduce the angular frequency from the fit of this signal. The problem is, that for small rotation angles, such as the ones we aim to measure, the beating will be so slow, that the signal will have died out before we have had the chance to observe any maxima or minima, making our fits unreliable. We tackle this problem further below.

1.4 Mode Matching

In order for a cavity to work, it must be properly mode-matched. Up to this point we have ignored the fact that due to the Gaussian nature of light, the beam tends get broader, especially if the length it traverses gets much larger than the Rayleigh length. In a cavity such as the ones that we use, we aim to have more than a hundred rounds trips, making the beam path, kilometer long. We would expect that after a few round trips, the beam waist would become larger than the mirrors themselves and thus escape. In order to avoid this, we must mode-match our setup. That is, the radius of curvature of the beam must match the curvature must match the radius of curvature at the mirrors.

This is achieved in two stages. We first choose proper lenses at proper distances before the cavity, so as to make sure that the curvature of the beam matches the curvature of the input coupler at the point where they meet. In our case the input coupler is flat, therefore the beam waist must coincide with the coupler position. Then, inside the cavity, we use a mix of flat and spherical mirrors in order to always match the radius of curvature.

The mathematical handling of this problems makes use of the ABCD law. Some details are due. Supposing a geometrical optics, a light wave can be described by a 2-vector containing its position and inclination. Thus:

$$\boldsymbol{E} = \begin{pmatrix} r \\ r' \end{pmatrix} \quad (1.4.1)$$

The effect of each optical element can be described with as 2x2 matrix. We will need the matrices for reflection by mirror and free space propagation. Some straightforward geometrical manipulations yield:

$$M = \begin{pmatrix} 1 & 0 \\ -2/R & 1 \end{pmatrix} \quad (1.4.2)$$

$$P = \begin{pmatrix} 1 & d \\ 0 & 1 \end{pmatrix} \quad (1.4.3)$$

Thus if the radius of curvature of the mirrors are $\{R_i\}$ and the length of the cavity arms are d_1 an d_2, then the matrix describing a round trip around the cavity is:

$$L = M(R_1)P(d1)M(R_2)P(d_2)M(R_3)P(d_1)M(R_4)P(d_2) = \begin{pmatrix} A & B \\ C & D \end{pmatrix} \quad (1.4.3)$$

We can act with this matrix on the input ray, and find its position and inclination after one (or more if we act again) round trip. In order to have a repetitive path, the following condition must hold true:

$$LE = E \quad (1.4.4)$$

In reality we deal with Gaussian beams, therefore curvature and beam diameter must be also taken into account. We define the complex beam parameter q:

$$\frac{1}{q} = \frac{1}{R} - i\frac{\lambda}{\pi w^2} \quad (1.4.5)$$

The ABCD law states that if we have an initial beam of q_1, that traverses through a bunch of optics, the final complex beam parameter q_2 will be given by:

$$\frac{1}{q_2} = \frac{C+D/q_1}{A+B/q_1} \quad (1.4.5)$$

In order for our cavity to be mode matched, the complex beam parameter must remain the same, i.e. $q_2 = q_1$ which yields the following conditions (taking into account that L must be unitary):

$$Cq^2 + (D-A)q - B = 0 \quad (1.4.6)$$

$$AD - BC = 1 \quad (1.4.7)$$

This system of equations is overdefined, and thus can be satisfied by multiple sets of parameters A,B,C and D, thus there are multiple mirror and distance setups that guarantee mode-mathcing.

Of course, despite our best efforts, it is impossible to have perfect mode matching. In order to have a perfect mode matching, the cavity must be matched for all TE$M_{m,p}$ modes. Best case scenario, we are able perfectly-ish match for the first few low lying TEM modes. The light emitted by the laser is of the form:

$$E = TEM_{00} + \varepsilon \sum_{m,p\neq 0} TEM_{m,p} \quad (1.4.8)$$

with $\varepsilon \ll 1$. If we have perfectly matched just the lowest mode, then the $TEM_{0,0}$ component will remain invariant after each round trip, whereas the rest of the modes will diverge after just a few round trips. This gives rise to what we call modal beating, which stains our signals. This can be seen in Figure:

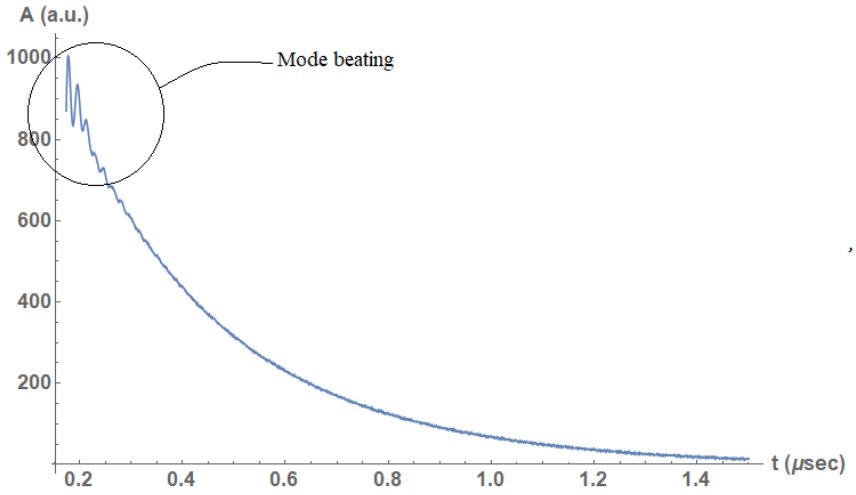

Figure 7: Signal with mode beating

The first two peaks occur due to modal beating. This problem will be tackled later on when we talk about data analysis.

One last thing to consider when building the cavity, is the fact that due to the pulsed nature of the laser we use, we must avoid self-coherences. Thus the round trip time of the pulse must be at least two times larger than its Full Width at Half Maximum (FWHM).

1.5 Circular Birefringence

Circular birefringence is the phenomenon of a material having different refractive indices for the right hand polarization (r.h.p.) and the left hand polarization (l.h.p.). Let 's call these indices n_+ and n_- correspondingly and examine their effect on linearly polarized light. We shall choose light polarized on the x-axis, therefore:

$$\boldsymbol{E}_{in} = \begin{pmatrix} 1 \\ 0 \end{pmatrix} \quad (1.5.1)$$

In order to observe the effect of circular birefringence, we must analyze the linear polarization into a linear combination of r.h.p and l.h.p. using the fact that:

$$\boldsymbol{E}_{rhp} = \frac{1}{\sqrt{2}}\begin{pmatrix} 1 \\ -i \end{pmatrix}, \ \boldsymbol{E}_{lhp} = \frac{1}{\sqrt{2}}\begin{pmatrix} 1 \\ i \end{pmatrix} \quad (1.5.2)$$

We get:

$$\boldsymbol{E}_{in} = \frac{1}{\sqrt{2}}\left(\boldsymbol{E}_{rhp} + \boldsymbol{E}_{lhp}\right) \quad (1.5.3)$$

After propagating in a circularly birefrigent medium with length d, each field component picks up a phase:

$$\boldsymbol{E}_{out} = \frac{1}{\sqrt{2}}\left(\boldsymbol{E}_{rhp}e^{ikn_+d} + \boldsymbol{E}_{lhp}e^{ikn_-d}\right) = \frac{1}{2}\begin{pmatrix} e^{ikn_+d} + e^{ikn_-d} \\ -ie^{ikn_+d} + ie^{ikn_-d} \end{pmatrix} = e^{ik(n_+ + n_-)d}\begin{pmatrix} cos\left[\frac{k(n_+ - n_-)}{d}\right] \\ sin\left[\frac{k(n_+ - n_-)}{d}\right] \end{pmatrix} \quad (1.5.4)$$

Therefore the output field, is the input field rotated by $\theta = \frac{k(n_+ - n_-)}{d}$.

Thus the effect of circular birefringence on linearly polarized light, is an optical rotation proportional to the difference of the refractive indices. The rotations we aim to measure are a product of circular birefringence, the source of which will be examined further below.

Having seen the effect of circular birefringence we can prescribe a Jones matrix to any circularly birefringent material:

$$M_{cb} = e^{-ad}\begin{pmatrix} cos\left[\frac{k(n_+ - n_-)}{d}\right] & -sin\left[\frac{k(n_+ - n_-)}{d}\right] \\ sin\left[\frac{k(n_+ - n_-)}{d}\right] & cos\left[\frac{k(n_+ - n_-)}{d}\right] \end{pmatrix} \quad (1.5.5)$$

With this matrix in hand, it determining the effect of circular birefringence on any potential polarization becomes trivial. We have added an exponentially decaying factor in order to account for any potential light absorption, but it will usually be set to unity.

1.6 Linear Birefringence

Linear birefringence is an effect similar to the circular one, with the main difference being that, there now exist two perpendicular axes with different refractive indices. Let's suppose that the fast axis coincides with the horizontal axis and the slow axis with the perpendicular one. The refractive indices are n_1 and n_2 respectively.

Suppose that our initial field has linear polarization at angle θ with respect to the horizontal axis:

$$\boldsymbol{E}_{in} = \begin{pmatrix} cos\theta \\ sin\theta \end{pmatrix} \quad (1.6.1)$$

We must analyze the polarization into the fast and slow axis components:

$$\boldsymbol{E}_{in} = \begin{pmatrix} cos\theta \\ sin\theta \end{pmatrix} = cos\theta\boldsymbol{E}_1 + sin\theta\boldsymbol{E}_2 \quad (1.6.2)$$

After the light, traverses distance d over a linearly birefringent medium, each component picks up a phase, thus:

$$\boldsymbol{E}_{out} = cos\theta \boldsymbol{E}_1 e^{ikn_1 d} + sin\theta \boldsymbol{E}_2 e^{ikn_2 d} = e^{ikn_1 d} \begin{pmatrix} cos\theta \\ sin\theta e^{ik(n_2 - n_1)d} \end{pmatrix} \sim \begin{pmatrix} cos\theta \\ sin\theta e^{i\varphi} \end{pmatrix} \quad (1.6.3)$$

Therefore linear birefringence transforms light with linear polarization to light with elliptical polarization. It is important to note that if the initial polarization coincides with either the fast or the slow axis, then one of the components of $\boldsymbol{E}_{out}$ vanishes and the polarization remains linear.

We can prescribe a Jones matrix to linearly birefringent media:

$$M_{lb} = e^{-ad} \begin{pmatrix} e^{ikn_1 d} & 0 \\ 0 & e^{ikn_2 d} \end{pmatrix} \quad (1.6.4)$$

Same as before we multiply by an exponentially decaying factor in order to account for potential absorption. In order to get the Jones matrix for arbitrary fast and slow axis, we have make a similarity transformation with rotation matrices, that is:

$$M_{lb}(\theta) = R(-\theta) M_{lb} R(\theta) \quad (1.6.5)$$

In Figure 8 we can see the effect of both kinds of birefringence, on an initially linearly polarized field.

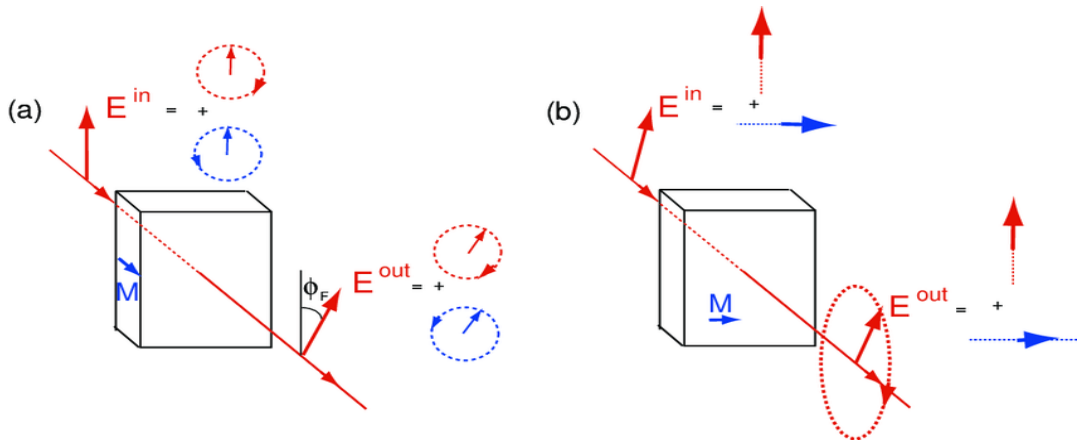

Figure 8: a)Effect of circular birefringence, b)effect of linear birefringence. Image extracted from Ultrafast light-induced dynamics of spins and lattice in iron oxides, Alexandra M Kalashnikova

1.7 Sources of birefringence

Firstly, the cavity we use, consists of four mirrors, thus any one of them can be out of the plane defined by the rest of them. This non planarity gives rise to optical rotation due to circular birefringence.

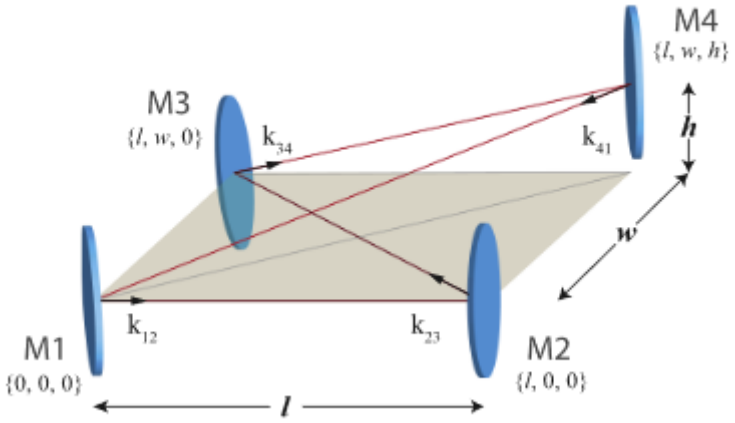

Figure 9: Non planar bowtie cavity. Image extracted from Chiral cavity ring down polarimetry: Chirality and magnetometry measurements using signal reversals, Lykourgkos Bougas et al.

The rotation angle per pass is:

$$sin\alpha_c = 2\frac{-l+\sqrt{l^2+w^2}}{w} tan^{-1}(h/l) \quad (1.7.1)$$

Another source of birefringence, is the angle at which the light is reflected on each mirror. According to Fresnel equations, whenever the angle of incidence exceeds the critical angle, then linear birefringence is introduced. In our case, the optics we use are multi-layered which leads to birefringence at even smaller angles. Empirically, whenever lights gets reflected at angles greater than a few degrees, a great amount of birefringence is introduced. Thus a certain amount of care must be taken when designing the cavity, so that the angles of incidence remain low, roughly less than 5^o.

Perhaps the main source of birefringence in our case, is a CeF_3 crystal that we use in order to achieve Faraday rotations (described further below). Whenever the light, traverses this crystal following a path that is not parallel to the axis of the crystal, the light picks up enormous amounts of linear birefringence, and thus great care must be taken when setting up the light path.

Finally birefringence can be introduced due to external fluctuations that perturb the cavity itself in random ways, which can range from dust molecules in the light path, to vibrations due to people walking or talking nearby the cavity.

Since it is apparently impossible to fully eliminate all sources of birefringence, we have developed a technique based on large Faraday rotations, which minimizes the problems caused by it, and is described below

1.8 Faraday effect

The Faraday effect, discovered be Michael Faraday (as the name implies) is a phenomenon that couples magnetic fields in materials and light propagating through them, More specifically, when light propagates trough a medium and at the same a collinear magnetic field is applied, an optical rotation is produced. Suppose that the light propagates through a medium of length *d*, and that the direction of propagation is along the z-axis. If we apply a magnetic field $\boldsymbol{B}(z) = f(z)\hat{z}$ then the Faraday rotation is:

$$\varphi_F = \int_0^d V f(z) dz \quad (1.8.1)$$

Where V is a constant of the material called Verdet constant. Using the semi-classical atomic model where electrons are bound to atoms with spring-like forces, H. Becquerel was able to derive a formula for the Verdet constant:

$$V = \frac{dn}{d\lambda}\frac{\lambda}{2c^2}\frac{q}{m} \quad (1.8.2)$$

One important thing about Faraday rotation is that, it has non-reciprocal nature. This means that the angle of rotation, and more specifically its sign, is independent of the direction of propagation of the light, i.e. the rotation has always the same sign in the lab frame. This is due to the fact that the fast and slow phase components, are defined by the applied magnetic field, which remains the same, irrespective of the direction of propagation. This becomes quite clear in Figure 11:

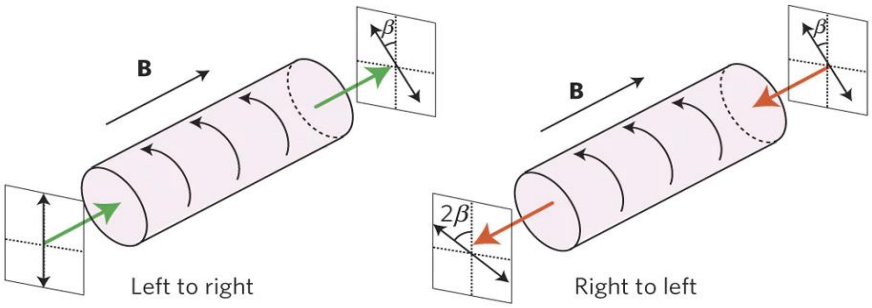

Figure 10: Non-reciprocity of Faraday effect. Image extracted from https://www.fiberoptics4sale.com/blogs/wave-optics/99205446-faraday-effect

1.9 Chirality

We shall now change rhythm and talk in more depth about a much more fundamental concept in (but certainly not only) physics. We will talk about the concept of chirality, which is in the heart of this thesis.

Chirality is a form of asymmetry prevalent in nature from the smallest to the largest scale. The term chiral was introduced by Lord Kelvin, and was used to describe an object that does not coincide with its mirror image. The word chiral is derived from the greek word "χειρ" meaning hand, since our hands are the most obvious objects that display such asymmetry.

Our hands are mirror images of one another, and it takes but a moment to reassure ourselves that they indeed cannot coincide. Therefore our hands are chiral. This can be made even more obvious in the following Figure:

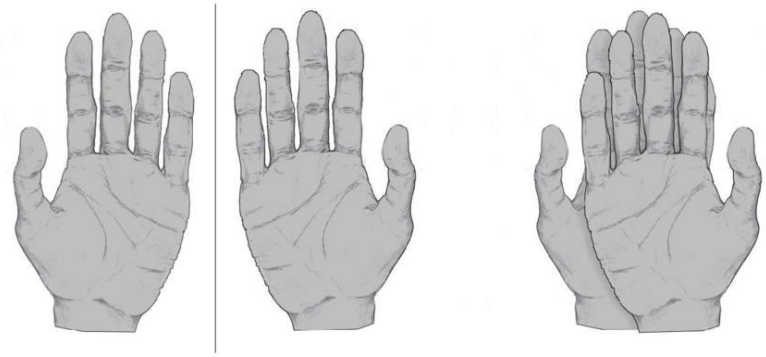

Figure 11: The chiral nature of hands. Image extracted from Synthesis of enantiomerically pure helical aromatics such as NHC ligands and their use in asymmetric catalysis. Manfred Karras

As mentioned above chirality a characteristic prevalent in all scales of nature. At the smallest scale, the fundamental weak nuclear force is itself chiral, since the interactions governed by it depend on electron helicity. Moving up, any molecule that contains more than a few atoms, tends to be chiral, such an example is 1-chloroethanol shown in Figure 12:

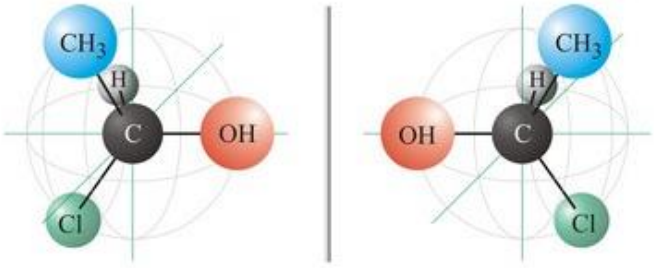

Figure 12: 1-chloroethanol and its mirror image. Image extracted from https://glossary.periodni.com/dictionary.php?en=chiral+molecule

Proceeding to larger scales, we can observe that the phenomenon of life itself is inherently chiral, due to the structure of our DNA which forms a chiral helix. Helical patterns are also found in multiple plants and oyster shells and so forth. Finally galaxies themselves tend to be chiral, with the most obvious example being the spiral galaxies.

One result of molecular chirality, is molecular optical activity which we aim to measure. Let us see how optical activity emerges from chirality. We follow the derivation presented in the book Chiral Analysis, P.A. Polvarapu.

Suppose we have circularly polarized light. It follows, that the EM field will be described as:

$$\boldsymbol{E}_{\pm} = \frac{E_0}{\sqrt{2}}(\hat{x} \mp i\hat{y}) \quad (1.9.1)$$

$$\boldsymbol{B}_{\pm} = \frac{B_0}{\sqrt{2}}(\pm\hat{x} + i\hat{y}) \quad (1.9.2)$$

"+" corresponds to r.h.p. and "-" to l.h.p.

The light traverses, in our case, through a gas, the molecules of which we will describe as a two state system, with the states being $|\Psi_g\rangle$ and $|\Psi_e\rangle$, corresponding to the ground and excited state. When an EM field is applied, there occur two main types of transition, electric dipole (E1) and magnetic dipole (M1). We denote the dipole moment operators as **E1** and **M1** respectively. The expression for these operators are:

$$\boldsymbol{E1} = \sum_{\boldsymbol{i}} e\boldsymbol{r}_i \quad (1.9.3)$$

$$\boldsymbol{M1} = -\frac{e\hbar}{2m_e c}(\boldsymbol{L} + 2\boldsymbol{S}) \quad (1.9.4)$$

The E1 transition operator is $H_{E1} = \boldsymbol{E1} \cdot \boldsymbol{E}$ and the M1 transition operator is $H_{M1} = \boldsymbol{M1} \cdot \boldsymbol{B}$. These two types of transitions obey different selection rules. More specifically E1 transitions apply when the transition changes the parity of the wavefunction, i.e. from even to odd or from odd to even. On the contrary M1 preserves the parity of the wavefunction, i.e. from even to even and from odd to odd. In a achiral molecule, the molecular states are entirely separated into even and odd states. Thus any transition is either purely E1 or M1. When this applies, the transition amplitudes are the same, independently of the polarization:

$$|H_{E1}|^2 = \left|\langle\Psi_e|\boldsymbol{E1} \cdot \boldsymbol{E}_+|\Psi_g\rangle\right|^2 = \left|\langle\Psi_e|\boldsymbol{E1} \cdot \boldsymbol{E}_-|\Psi_g\rangle\right|^2 \quad (1.9.5)$$

$$|H_{M1}|^2 = \left|\langle\Psi_e|\boldsymbol{M1} \cdot \boldsymbol{B}_+|\Psi_g\rangle\right|^2 = \left|\langle\Psi_e|\boldsymbol{M1} \cdot \boldsymbol{B}_-|\Psi_g\rangle\right|^2 \quad (1.9.6)$$

In the case of a chiral molecule, the molecular states do not have well defined parity. Instead each state is a superposition of an odd and an even state. Therefore the transitions themselves are not purely E1 and M1, but a mix of those two. Thus the transition operator becomes:

$$H_{\pm} = \boldsymbol{E1} \cdot \boldsymbol{E}_{\pm} + \boldsymbol{M1} \cdot \boldsymbol{B}_{\pm} \quad (1.9.7)$$

And the transition amplitude is:

$$A_{\pm} = \left|\langle\Psi_e|\boldsymbol{E1} \cdot \boldsymbol{E}_{\pm} + \boldsymbol{M1} \cdot \boldsymbol{B}_{\pm}|\Psi_g\rangle\right| \quad (1.9.8)$$

By expanding the field terms, we observe that the transition amplitudes vary depending on the polarization, that is:

$$A_+ = \left|\left\langle\Psi_e|\boldsymbol{E1} \cdot \frac{E_0}{\sqrt{2}}(\hat{x} - i\hat{y}) + \boldsymbol{M1} \cdot \frac{B_0}{\sqrt{2}}(\hat{x} + i\hat{y})|\Psi_g\right\rangle\right| = \left|\left\langle\Psi_e|\frac{E_0}{\sqrt{2}}(E1_x - iE1_y) + \cdot\frac{B_0}{\sqrt{2}}(M1_x + iM1_y)|\Psi_g\right\rangle\right| =>$$

$$A_+ = \frac{E_0}{\sqrt{2}}\left[\left(E1_x^{eg} + \frac{1}{c}M1_x^{eg}\right) + i\left(-E1_y^{eg} + \frac{1}{c}M1_y^{eg}\right)\right] \quad (1.9.9)$$

$$A_- = \left|\left\langle \Psi_e | \boldsymbol{E1} \cdot \frac{E_0}{\sqrt{2}}(\hat{x} + i\hat{y}) + \boldsymbol{M1} \cdot \frac{B_0}{\sqrt{2}}(-\hat{x} + i\hat{y}) | \Psi_g \right\rangle\right| = \left|\left\langle \Psi_e | \frac{E_0}{\sqrt{2}}(E1_x + iE1_y) + \frac{B_0}{\sqrt{2}}(-M1_x + iM1_y) | \Psi_g \right\rangle\right| =>$$

$$A_- = \frac{E_0}{\sqrt{2}}\left[\left(E1_x^{eg} - \frac{1}{c}M1_x^{eg}\right) + i\left(E1_y^{eg} + \frac{1}{c}M1_y^{eg}\right)\right] \quad (1.9.10)$$

Thus the transition probabilities differ for r.h.p. and l.h.p. The normalized difference in transition probabilities is:

$$\delta = \frac{|A_+|^2 - |A_-|^2}{|A_+|^2 + |A_-|^2} = \frac{2Im[H_{E1}H_{M1}]}{|H_{E1}|^2 + |H_{M1}|^2} \approx 2Im\left[\frac{H_{M1}}{H_{E1}}\right] \equiv 2R \quad (1.9.11)$$

This ratio is a molecular constant that ranges from 10^{-3} to 10^{-6}. It is known as the asymmetry factor, and it 's a measure of "how" chiral a molecule is. The transition amplitudes are directly related with the absorption coefficient α(λ). We can use the Kramers-Kronig relation to derive the refractive indicices:

$$n(\lambda) = 1 + \frac{1}{2\pi^2} P \int_0^{+\infty} \frac{a(\lambda')}{1 - \left(\frac{\lambda'}{\lambda}\right)^2} d\lambda' \quad (1.9.12)$$

We can manipulate this relation to get:

$$\frac{n_+ - n_-}{n - 1} = \frac{|A_+|^2 - |A_-|^2}{|A|^2} \quad (1.9.13)$$

Where $n = \frac{n_+ - n_-}{2}$ and $|A|^2 = \frac{|A_+|^2 - |A_-|^2}{2}$. Thus chirality gives rise to circular birefringence, and thus optical rotation. This optical rotation is known as chiral rotation and differs in nature to the Faraday rotation.

Chiral rotation has reciprocal nature, that is the sign of the rotation depends on the direction that the light traverses the sample as show in figure 14:

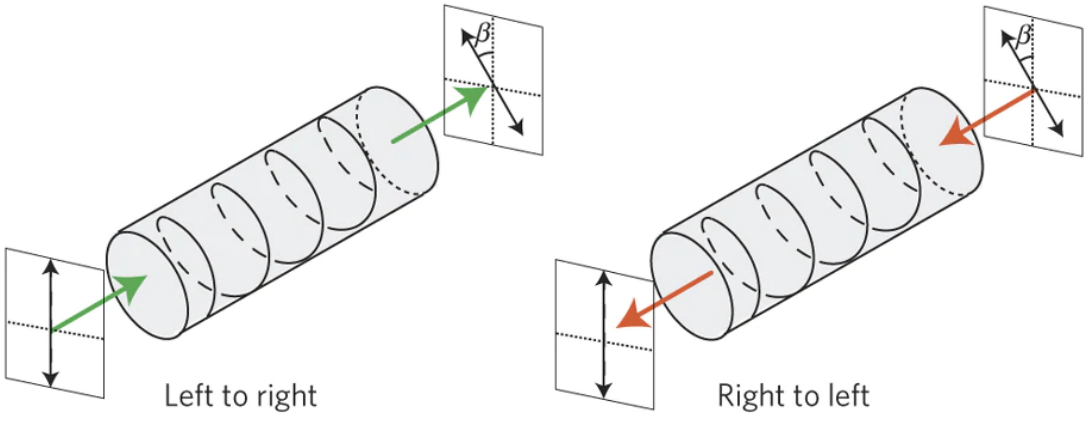

Figure 13: Reciprocal nature of chiral rotation. Image extracted from https://www.fiberoptics4sale.com/blogs/wave-optics/99205446-faraday-effect

The reciprocal nature of this rotation restricts the types of cavities we can use. More specifically, we are forced to use running cavities, so that the light always follows the same direction when passing through the sample. If we had used a standing cavity, the light would

pass through the sample twice per pass, following opposite direction, and thus the net chiral rotation would be zero.

There are ways to measure chiral rotation using standing cavities, but retarding wave plates must be employed, which lower the ringdown time of the signal due to imperfect transmitivity, and thus lower our level of certainty in frequency determination. Due to these considerations we have chosen to use a bowtie cavity, so that the polarization of the light picks up the same angle of rotation per pass without the need for any further optical elements.

1.10 Optical activity variation

Up to this moment, we have been talking in terms of the chiral rotation angle. This depends on multiple factors such as the kind of molecule that produces the rotation, the length of the path traversed by the pulse etc.

In order to avoid these ambiguities, we can define a new measure α called optical activity. This is defined using the following relationship

$$\varphi_c = adc \quad (1.10.1)$$

Where d is the length traversed by the pulse within the optically active medium, and c is the concetration of the chiral substance.

Optical activity is customarily measured in $[\alpha] = \frac{degrees}{dm\,\frac{gr}{ml}}$. By talking in terms of optical activity, we remove the setup specific parameters. Even so, it still is not a constant but has dependencies on wavelength and temperature.

An experimental formula for optical activity is:

$$[a]_\lambda^T = \frac{A_1^T}{\lambda^2 - \lambda_1^2} \quad (1.10.2)$$

Where λ_1 is some reference wavelength and A_1^T a parameter with weak temperature dependence. Typically the dependence on temperature, accounts only for very slight shifts, in optical activity. Even so, it can become important, since we use a specific wavelength laser, whereas the room temperature can shift from day to day.

In the following figures, we can observe the aforementioned dependencies:

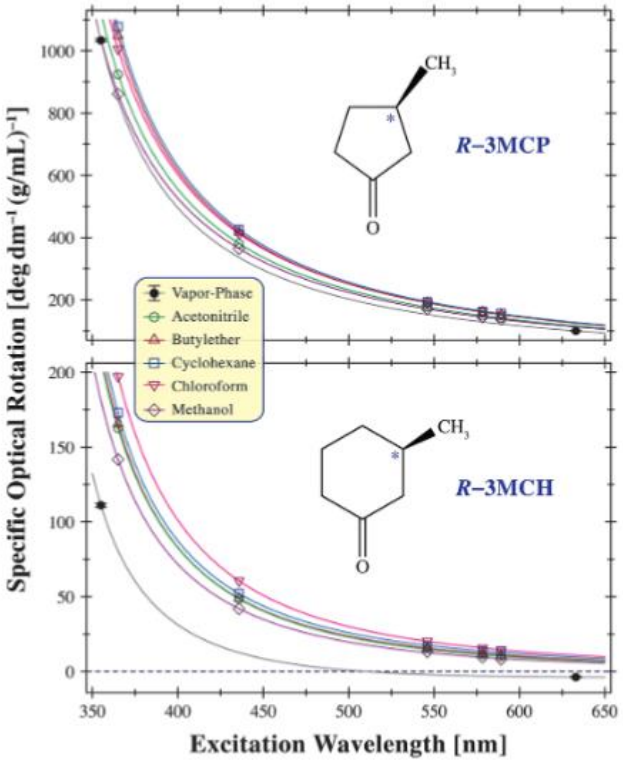

Figure 14: Wavelength dependence of Optical activity. Image Extracted from Intrinsic Optical Activity and Conformational Flexibility: The Role of Size-Dependent Ring Morphology in Model Cycloketones, Priyanka Lahiri, et. al

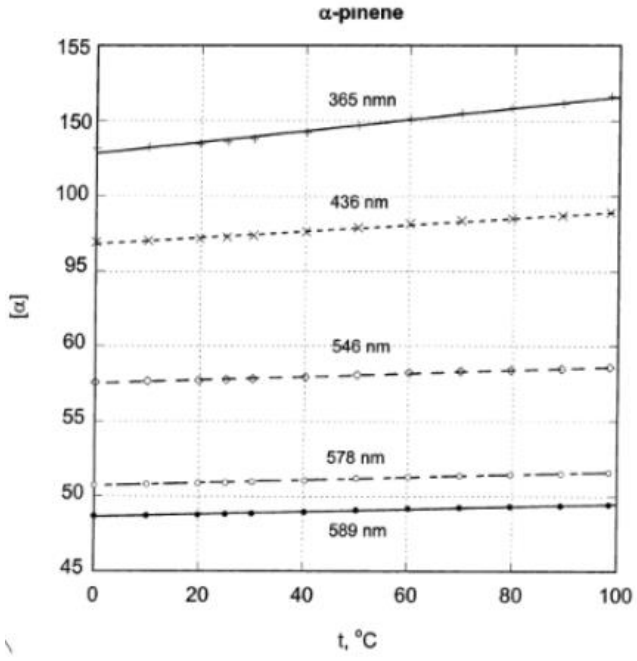

Figure 15: Optical activity dependence vs Temperature for a-pinene for various wavelengths. Image extracted from Temperature Dependence of Optical Rotation: α-Pinene, β-Pinene Pinane, Camphene, Camphor and Fenchone, Kenneth B. Wiberg et. al.

1.11 a-Pinene vapour pressure and optical activity

We shall now specifically refer to a-pinene, which is a chemical substance excreted by pine trees, especially when they get dents and cuts. This substance gives pine trees their characteristic smell.

Pinene is a chiral substance, whose optical activity we aim to measure. As mentioned before, optical activity is a function of both wavelength and temperature. We use the optical activity measurements performed by Vaccaro, and interpolate a reasonable curve, so as to approximate the optical activity at 532nm, which is the wavelength we operate on.

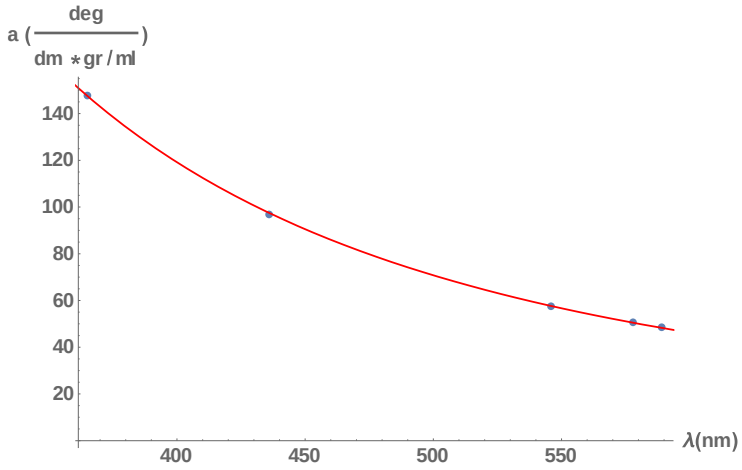

Figure 16: Optical Activity vs wavelength for a-pinene in room temperature

The derived optical activity at 532nm is $a = 61.2 \pm 5.2 \frac{deg}{dm \frac{gr}{ml}}$.

We aim to measure the chiral rotation occurring from a-pinene in the gas phase, therefore we need to know the vapour pressure at any given temperature. The formula extracted from NIST is:

$$P = 10^{3.92161 - \frac{1411.869}{T - 68.817}} \quad (1.11.1)$$

Where T is measured in Kelvins and P in bars. This formula is accurate for temperatures greater than 23°C. The vapour pressure plot (extracted from NIST) is presented in the following figure:

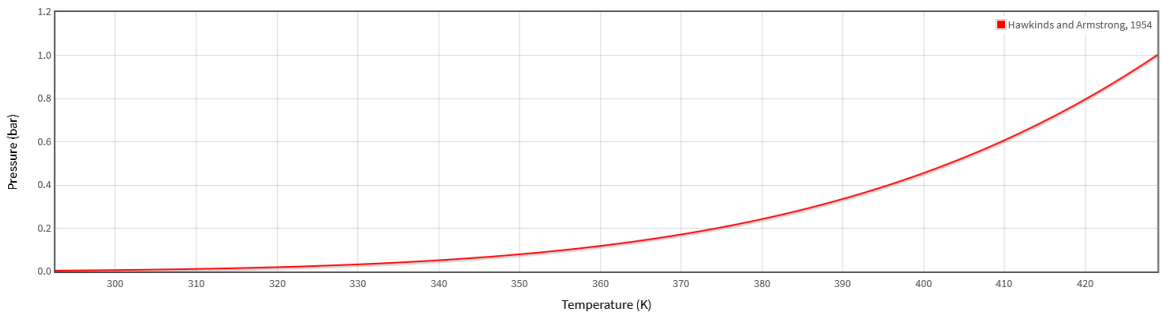

Figure 17: Vapour Pressure vs Temperature for liquid a-pinena

Chapter 2: Signal Analysis and Techniques

2.1 Effects of Linear Birefringence

Linear birefringence can be quite problematic in a CRDP experiment. The reasoning is simple. We want to measure the rotation angle by determining the beating frequency in our signals. If the polarization is elliptic, then the analyzer can never extinguish the entirety of the light, generating thus the signal troughs. If linear birefringence is present in our data, we are forced to make fits with more parameters and more complex forms, sacrificing thus accuracy in the parameter determination. We can demonstrate this by generating signals, with and without birefringence and trying to estimate the circular frequency. We also add Gaussian noise in most parametesr to make the signal more realistic. In Figure 18 we display three such signals with different fitting schemes.

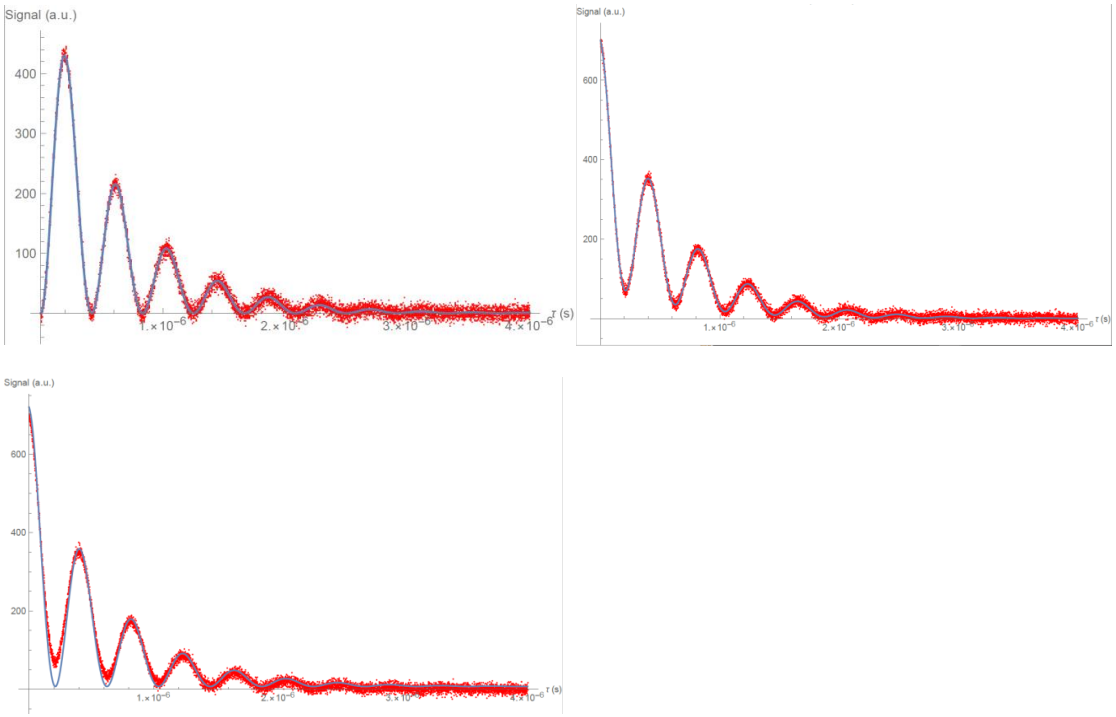

Figure 18: a)Signal without lb and fitted with 2.1.1 ,b)Signal with lb and fitted with 2.1.1, c)signal with lb and fitted with 2.1.2

The fitting functions we used are:

$$I_1 = Ae^{-\frac{t}{t}}cos^2(2\pi ft + \varphi) + B \quad (2.1.1)$$

$$I_2 = Ae^{-\frac{t}{t}}cos^2(2\pi ft + \varphi) + Be^{-t/\tau_b} + C \quad (2.1.2)$$

We ourselves generated the signals, therefore we already know the correct frequency to be f=1.2MHz. We can compare this with the fitted frequency for multiple iterations and get:

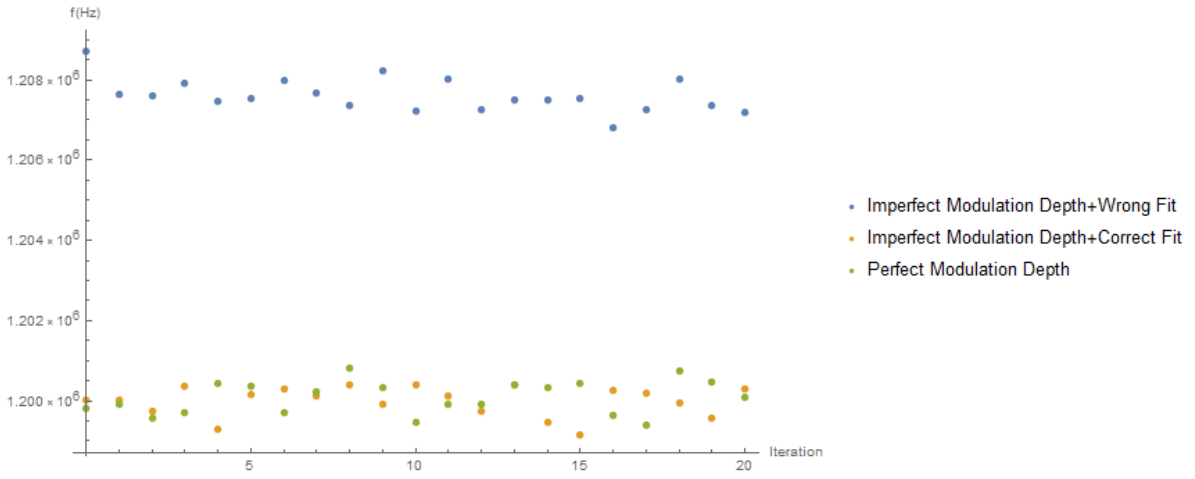

Figure 19: Frequency determination for the cases in Figure 7

We observe that cases a) and b) yield the correct frequencies, while case c) yield the correct frequency with a constant offset, which we are unable to predetermine in a real experiment. Therefore cases a) and b) seem equally viable at first glance. Even so, the results of case a) have better accuracy as can be seen in Figure 20.

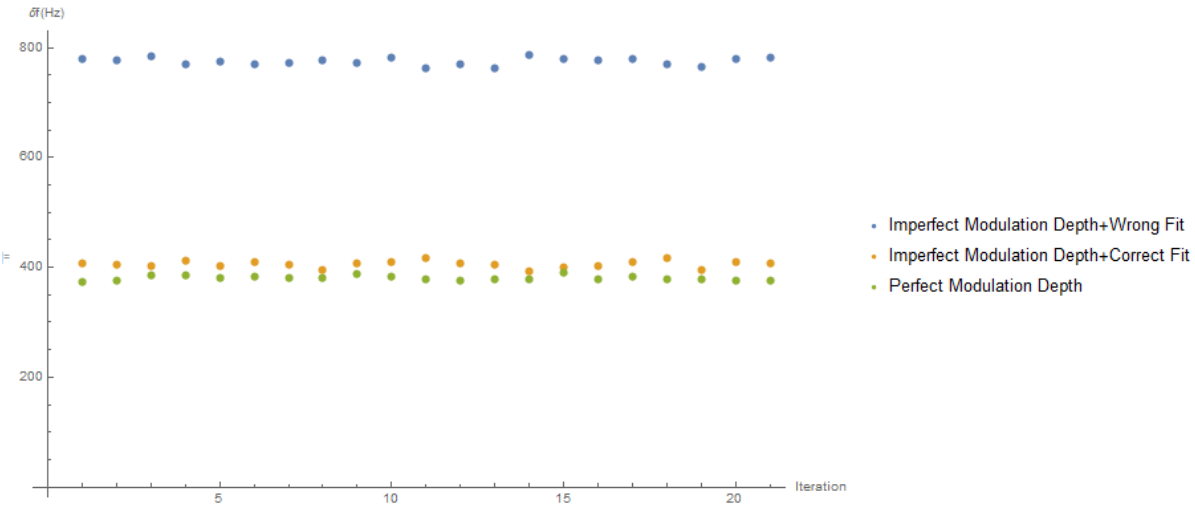

Figure 20: Error in frequency determination in the schemes presented in Figure 7

It is therefore obvious, that there is great merit to eliminating linear birefringence, since scheme a) yields consistently the best results. It is also favorable to eliminate any source of circular birefringence (besides the sample), so that we do not measure any form of polarization rotation, other than that of the sample. This in practice is nigh impossible, due to the reasons presented in chapter 1.7.

2.2 Error in frequency determination

We have made references to the error in the fitted frequency in our signals. We have already shown that linear birefringence negatively impacts the level of certainty in frequency determination, but this is only one of multiple parameters. If we ignore birefringence, the fitted signal is:

$$I_1 = Ae^{-\frac{t}{\tau_{RD}}}cos^2(2\pi ft + \varphi) + B \quad (2.2.1)$$

We now examine how the ringdown time and the amplitude of our light affects our estimates. We once again generate multiple signals, and insert Gaussian noise in all five fitted parameters. Each noise has a different characteristic timescale in order to account for the following effects.

The noise in amplitude and phase has a timescale same as the inverse repetition rate of our laser, in order to account for laser instability. The constant offset varies significantly over a few nanoseconds in order to simulate Johnson noise in our photodetection system. The variation in ringdown time is much slower (~100x inverse repetition rate) to account for vibrations that affect the mirror positioning. Finally we add a slow noise in frequency to simulate changes in Faraday rotation due to both heating effects from the coil that generates the magnetic field and dc current instability from its power supply.

The parameters that we have some control over, are the light amplitude and ringdown time. We can also increase or decrease beating frequency, by changing the dc current via the power supply.

We generate a series of signals with increasing ringdown time, and try to fit the aforementioned model. We then gather the error in beating frequency and repeat for a couple of different beating frequencies. The results are presented in Figure 21:

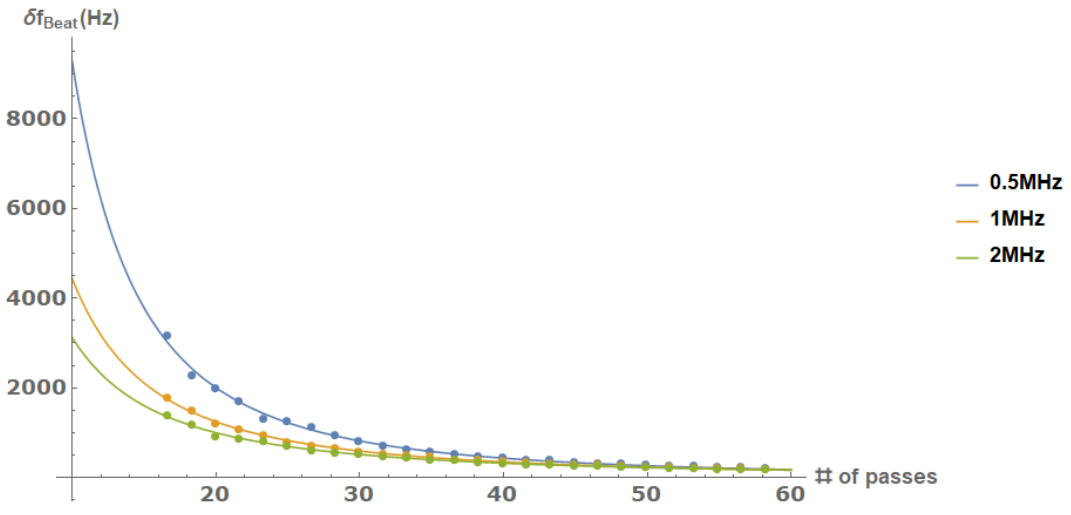

Figure 21: Error in beating frequency determination vs Ringdown time for various beating frequencies

We observe that δf gets better with both ringdown time and beating frequency, although the latter improvement becomes insignificant at higher ringdown times. This is quite reasonable since in order for the fit to be reliable, there has to be a decent number of peaks and troughs. After a sufficient number of peaks and troughs is present in the signal, adding more does not introduce any useful information and thus the error remains roughly the same. On the contrary increasing ringdown time seems more effective at reducing the uncertainty, due to the fact that same as before, more troughs and peaks are present, but also the signal gets more clear since variation in τ_{RD} becomes insignificant.

We perform the same process, but now instead of repeating over multiple beating frequencies, we repeat over multiple amplitudes. The result is straightforward and easy to guess. More light equals more information equals better fits. This is shown in Figure 22:

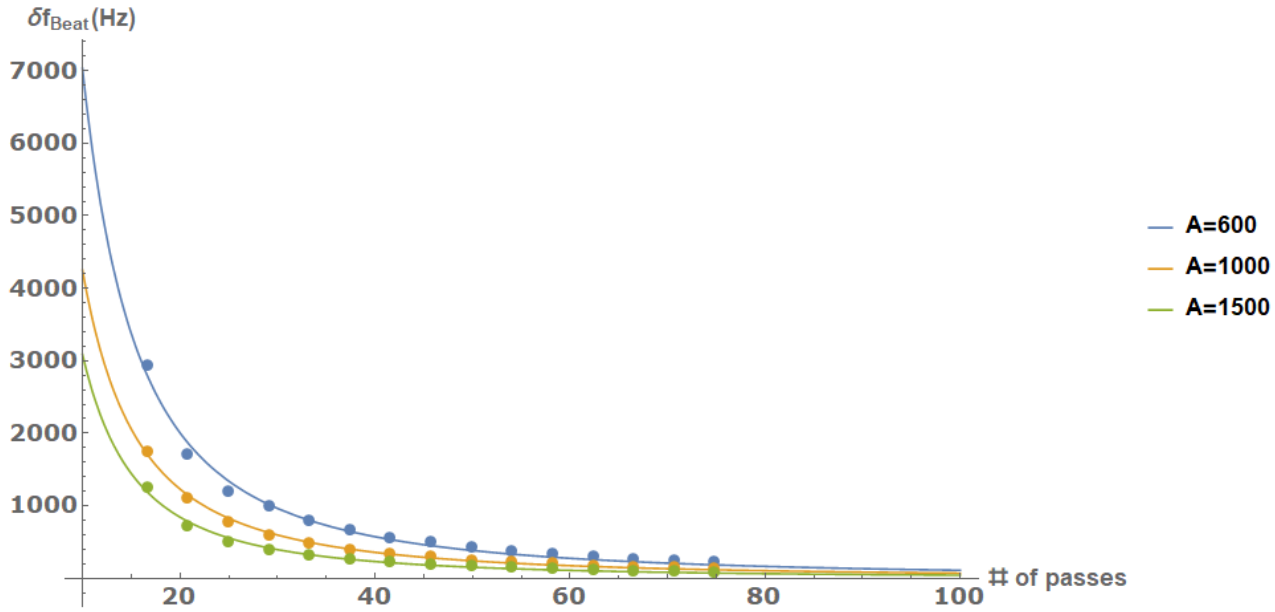

Figure 22: Error in beating frequency determination vs ringdown time for multiple light amplitudes

The result we draw is simple if not obvious, we must maximise both ringdown time and light amplitude in order to improve the accuracy of our instrument. This is not as simple as it may at first seem. The reason is, that in order for us to maximise the light amplitude, we must use input couplers of lower reflectivity. That in order reduces ringdown time since:

$$\tau_{RD} = \frac{t_{rt}}{1-e^{-ad}\prod_i R_i} \quad (2.2.2)$$

The optical component with the worst reflectivity (or absorbance) dominates. This is displayed in Figure 23:

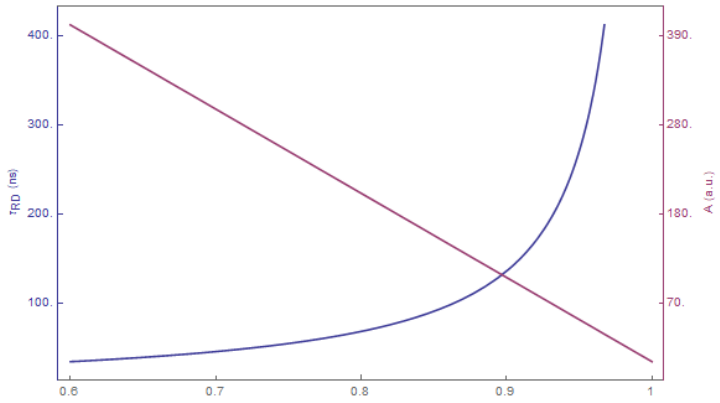

Figure 23: Ringdown time and light amplitude vs input coupler reflectivity

We have empirically observed that it is preferable to maintain the highest ringdown time possible, and work with whatever amplitude remains.

In order to further improve our accuracy and quench potential sources of noise or birefringence we employ a couple of tricks and techniques. More specifically we use pulse averaging, magnetic field reversals and two counterpropagating beams. The latter techniques will be developed further later on. For the time we will focus on pulse averaging.

The premise is simple, instead of measuring and analysing signals that occur from a single pulse traversing the cavity, we take signals emerging from the statistical average of a thousand consecutive pulses (using a high repetition rate pulsed laser). Due to the random nature of the noises, the signal tends to get much more clear after just a few averages. In Figure 24 we compare the signal from a single pulse vs the signal of the averaging of fifty pulses:

a) b)

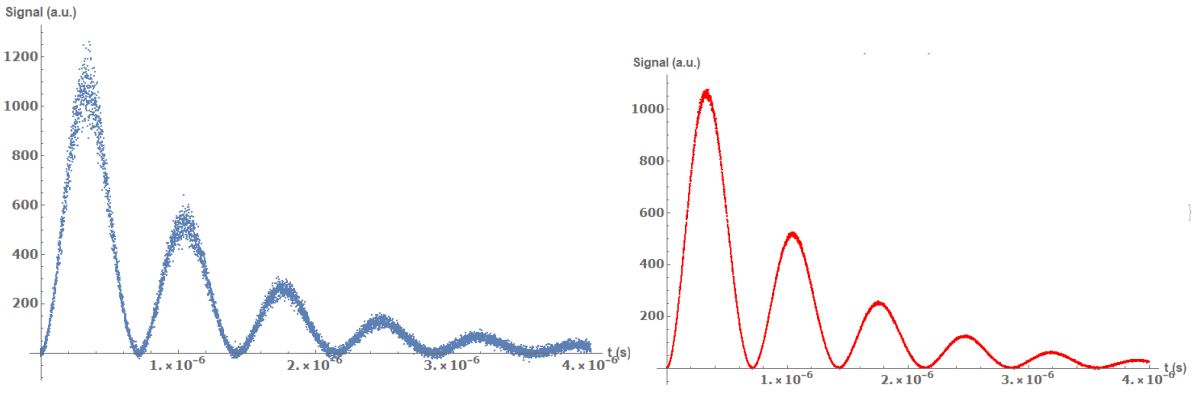

Figure 24: a) Signal from a single pulse, b) signal from 50 pulses

The peaks and troughs are much more clear, making thus the fit more reliable. More specifically the error in frequency determination drops following a $\frac{1}{\sqrt{Number\ of\ Pulses}}$ behaviour. This is displayed in Figure 25:

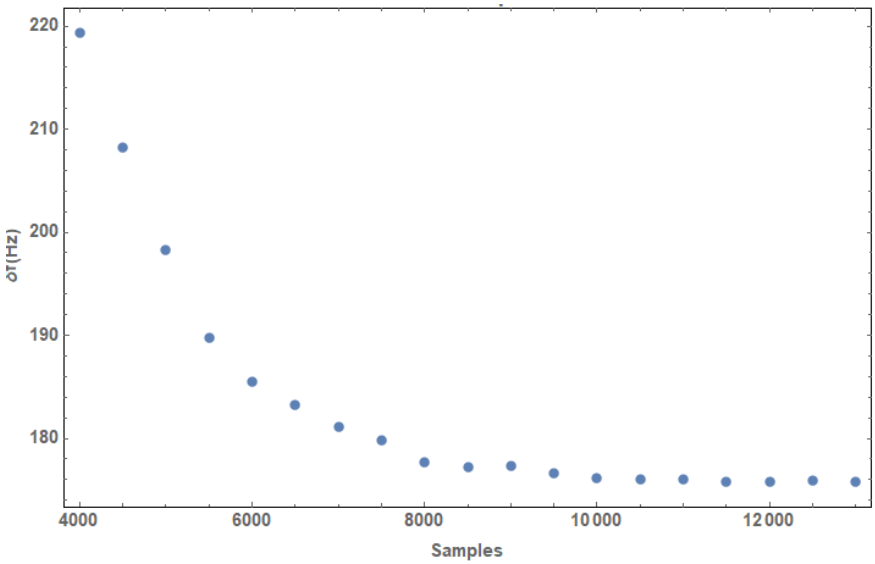

Figure 25: Error in frequency vs number of pulses averaged

One final refinement we perform, is to remove the first couple of hundreds nanoseconds from the signal, in order to eliminate any noise due to mode beating from the imperfect mode matching. Mode beating is apparent in a ringdown signal such as the one in Figure 26:

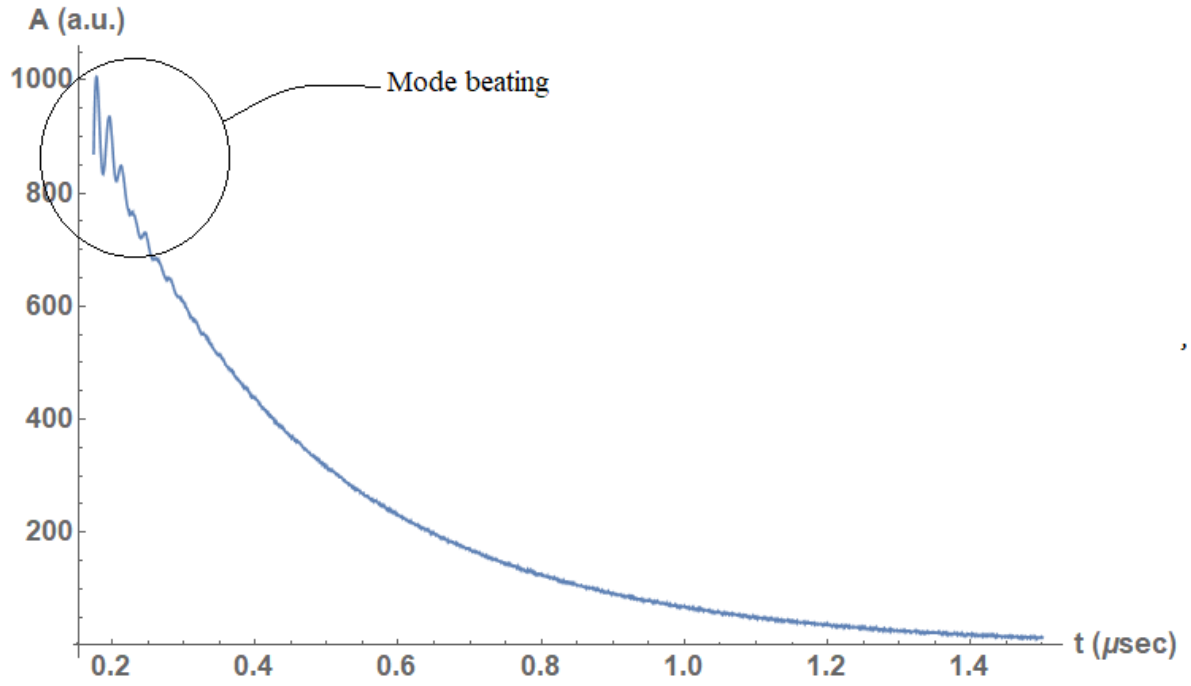

Figure 26 : Sample signal with mode beating present

By not including the first few hundred nanoseconds in the analysis, the signal becomes more clear and our fits more reliable. This can be done, as long as the ringdown time of the cavity is much larger than the time omitted, This is because, according to Figure 22: sacrificing ringdown time, also damages our accuracy. Therefore in each case, tests must be performed, so as to determine which scheme of analysis is preferable.

2.3 Quenching Linear Birefringence

In our setup, we aim to measure small (order microdegree) chiral rotations. As mentioned above, even small amounts of birefringence can be problematic, because instead of measuring the rotated component of the polarization that lies on top of the polarizer transmission axis, we measure the component due to elliptical polarization. This can be made obvious, if we introduce a small amount of linear birefringence in our cavity. Using Jones calculus we can get the light polarization after each pass. Suppose our initial polarization is on the x-axis and that the Fast Axis of the linear birefringence lies at θ = 45 degrees to the horizontal. Then the output field after each pass (ignoring absorption) is:

$$\boldsymbol{E}_{out}(k) = [M_{lb}(\theta, \delta n) M_{rot}(\varphi)]^k \boldsymbol{E}_{in} \quad (2.3.1)$$

For comparable chiral rotation and phase retardation, the polarization evolves as shown in Figure 27:

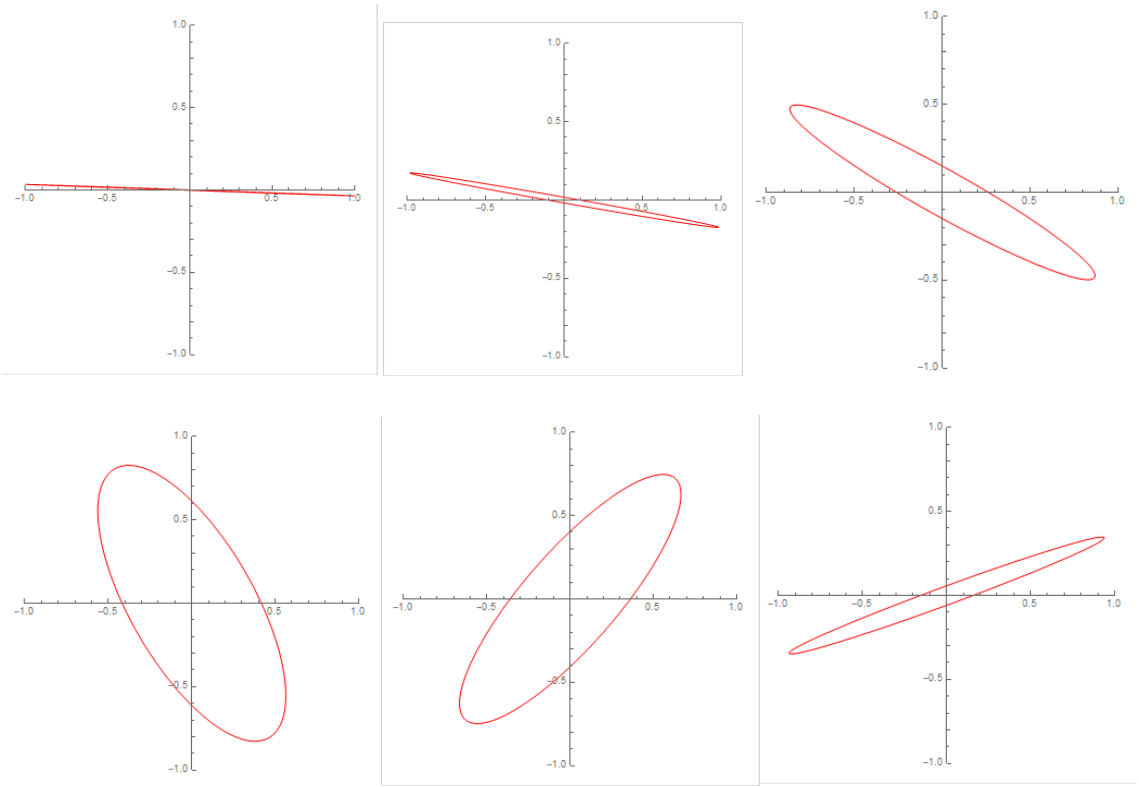

Figure 27: Time evolution of polarization with linear birefringence

It is obvious that the projection on the polarization axis is both affected by the rotation itself, and the ellipticity, making it impossible to discern which is which.

In order to quench the effects of ellipticity, we introduce a magneto-optical crystal, and apply a parallel magnetic field. This introduces a non-reciprocal Faraday rotation θ_F. We apply a strong enough field, so that $\theta_F \gg \varphi_c$. This shifts the beating frequency to $\omega = \frac{\theta_F + \varphi_c}{\tau_{rt}}$. Theoretically, as long as we know θ_F to infinite accuracy, the shift in frequency presents no

problem. In reality, due to instabilities of the magnetic field, this is impossible. This problem is tackled by using the reversal technique, explained later on.

By introducing a large Faraday rotation, the output field after each pass becomes:

$$\boldsymbol{E}_{out}(k) = [M_{lb}(\theta, \delta n) M_{rot}(\varphi_c) M_{rot}(\theta_F)]^k \boldsymbol{E}_{in} \quad (2.3.2)$$

The time evolution of the field polarization looks like this ($\theta_F = 10\varphi_c$):

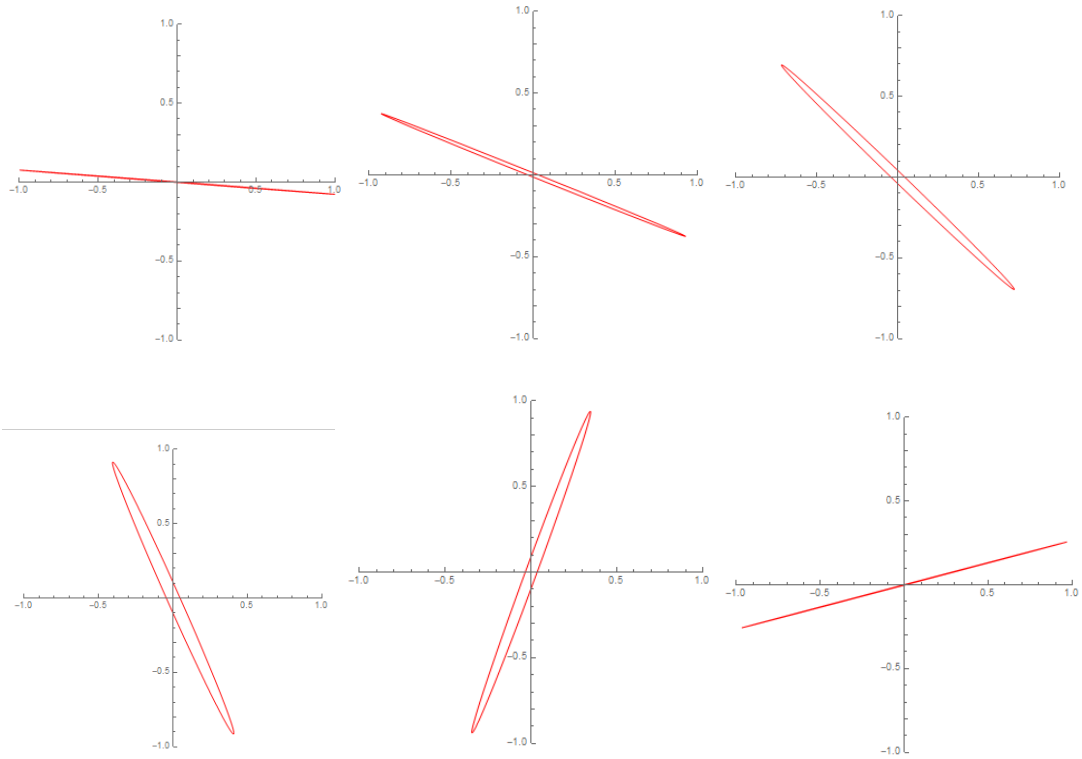

Figure 28: Time evolution of polarization with linear birefringence and Faraday rotation

From the last two figures, it becomes obvious that a large Faraday rotation, indeed quenches the effects of linear birefringence. In practices this technique is even more effective, because the Faraday rotation angle is ~3-4 orders of magnitude greater than the chiral angle, whereas in the figure it is just 28.

2.4 Counterpropagating beams

In the previous subsection we introduced a technique used to quench linear birefringence. This technique had the problem that it also introduced an optical rotation, that cannot be perfectly determined, even though we are the ones to generate it. In order to solve this problem, we introduce a second counterpropagating beam inside the cavity. This is done by utilizing the back-reflection from the input coupler and a carefully placed secondary mirror, to drive it back inside the cavity.

We shall henceforth call these two beams CW and CCW. The two beams traverse the magneto-optical crystal and the chiral sample in opposite directions, Both beams pick up the same Faraday optical rotation due to its non-reciprocal nature. On the contrary, they pickup the opposite chiral optical rotation, since it is reciprocal in nature. Therefore the polarization rotation per pass is:

$$a_{cw} = \theta_F + \varphi_c \; and \; a_{ccw} = \theta_F - \varphi_c \quad (2.4.1)$$

Two ringdown signals are generated from each pulse, with the respective beating frequencies being:

$$\omega_{cw} = \frac{\theta_F + \varphi_c}{\tau_{rt}} \; and \; \omega_{ccw} = \frac{\theta_F - \varphi_c}{\tau_{rt}} \quad (2.4.2)$$

By fitting both signals and deriving the beating frequencies we can derive the chiral rotation itself.

$$\varphi_c = (\omega_{cw} - \omega_{ccw})\tau_{rt}/2 \quad (2.4.3)$$

The merit of this technique is dual. First and foremost, the signals from two beams which traverse the cavity at the same time, experience the same sources of drifts and noises. Thus, by having two sets of signals, it is much easier to remove noises which have nanosecond timescales. Furthermore if for whatever reason there is a drift in beating frequency, it usually tends to be non-reciprocal, and thus the source of drift itself is removed, same as the Faraday rotation. Finally, this technique lifts the need to be able to accurately determine the Faraday rotation itself.

2.5 Magnetic Reversal

We employ one final refinement. Once we have collected a sufficient number of consecutive pulses, we reverse the direction of the magnetic field, reversing thus the sign of the Faraday rotation and repeat. One measurement is complete as soon as we have collected all four different signals. We derive four angular frequencies from their fits:

$$\omega_{cw}^{+} = \frac{\theta_F + \varphi_c}{\tau_{rt}} \; and \; \omega_{ccw}^{+} = \frac{\theta_F - \varphi_c}{\tau_{rt}} \quad (2.5.1)$$

$$\omega_{cw}^{-} = \frac{-\theta_F + \varphi_c}{\tau_{rt}} \; and \; \omega_{ccw}^{-} = \frac{-\theta_F - \varphi_c}{\tau_{rt}} \quad (2.5.2)$$

The signs in the exponents are used to differentiate between the two magnetic field directions. We can finally derive the chiral rotation:

$$\varphi_c = \frac{(|\omega_{cw}^{+}| - |\omega_{ccw}^{+}|) - (|\omega_{cw}^{-}| - |\omega_{ccw}^{-}|)}{4}\tau_{rt} \quad (2.5.3)$$

Magnetic field reversal also serves two purposes. Firstly, it helps to remove slowly varying noises, since it occurs after every couple of tenths of a second. Secondly it doubles the effect of the chiral rotation, since it is present in four signals instead of two.

Chapter 3: Experimental Setup and Apparatus

3.1 Setup

For all measurements and results presented in this chapter, we used the following setup. The cavity consists of two flat AR coated mirrors with reflectivity R=99.999% that act as input and output couplers, and two AR coated spherical mirrors with reflectivity R=99.999% and radius of curvature r=1.5m. The cavity round trip path is $L = 4.08m$. We are using a pulsed diode laser (RLTMPL-532-500-3-19042759) which produces 5.83ns pulses at a variable repetition rate of 1-10kHz, with a power of 554mW

In order to couple two counterpropagating beams inside the cavity, we used a back reflection mirror, so as to drive the initially reflected beam from the input coupler, back inside the cavity. Mode matching was achieved, using 2 lenses before the input coupler, and one extra lens on the reflection path, in order to correct for the path difference of the back-reflected beam. Due to the back-reflection, light from the beam redirects back to the laser, causing feedback effects. In order to avoid this, we introduced an in-home made isolator, consisting of a permanent cylindrical neodymium magnet and a TGG. The polarizers we used for the isolator where two Polarizing Beam Splitters (PBS). The diverging beam, from the second PBS was used in obtaining a trigger. Furthermore a HWP was used in order to extinguish any hints of ellipticity and a QWP in order to have minimize isolator light losses.

Inside the cavity we have placed a $d = 28cm$ gas cell, which serves to house our chiral gas sample. The cell is connected to an oil pump which can achieve a vacuum of 10^{-2}-10^{-3}mbar after a few minutes of use. In order to produce a Faraday rotation, we have built a multi-layer coil which houses a magneto-optic CeF_3 crystal. The coil current is controlled by a DC current generator (Delta Electronics), equipped with a relay, which can reverse the current direction when commanded by the PC. The coil itself, is connected with a cooling system, which circulates a mix of water and ethanol through the casing of the coil. This is done to avoid both thermal effects on the crystal and any coil parts melting due to high temperature. A schematic of the coil is presented in the next subchapter.

After the cavity, we have placed two analyzers on the path of the respective beams, with their transmission axis, perpendicular to the input polarization. Finally two lenses focus the beam onto the photodetector active surface (Thorlabs DET36). The signal is fed to our PC which is equipped with a Fast Data Acquisition Card (ADQ14DC-2X-PCIE) developed by Teledyne SP and custom recording software developed by Photek.

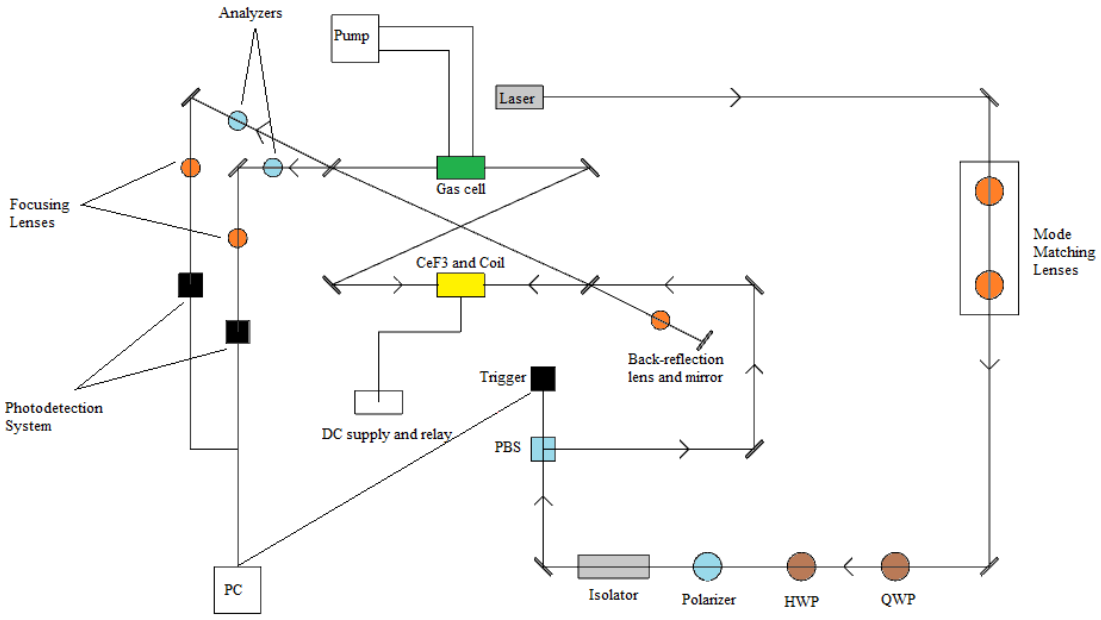

Figure 29: Experimental setup Schematic

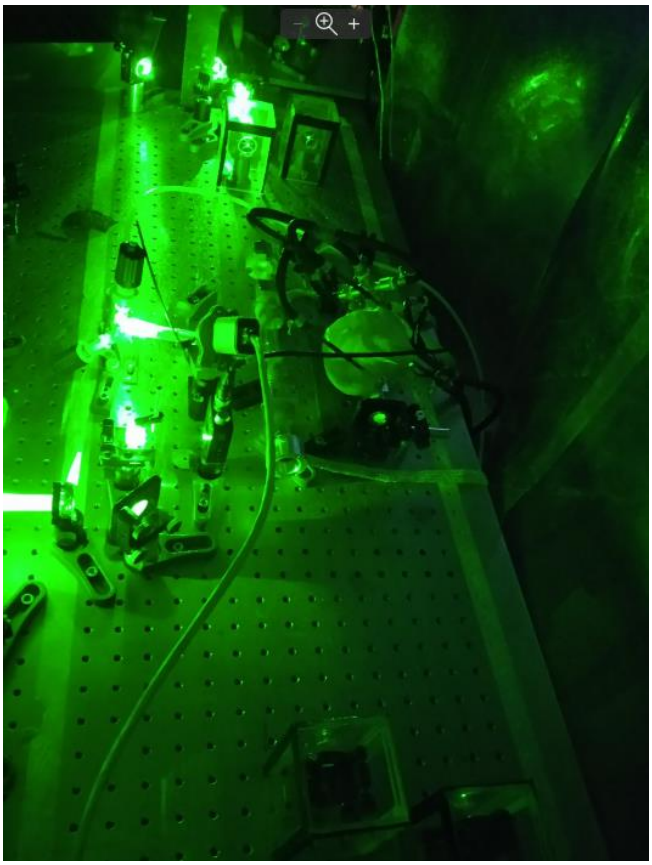

Figure 30: Photo of Experimental Setup

3.2 In-house made components

We now proceed to present, the two custom made components that were placed inside the cavity. First, we built a 18-layer, 30-turn coil. Between each layer, we placed thermal paste in order to effectively disperse heat from the inner layer towards the coolant outside. Furthermore electrically non-conductive and thermally conductive tape was place between certain layers. The coil was operated on a current of $I = 12A$, producing a field of roughly 1600G at its center, where the CeF_3 crystal was placed. We present, a schematic of the coil below.

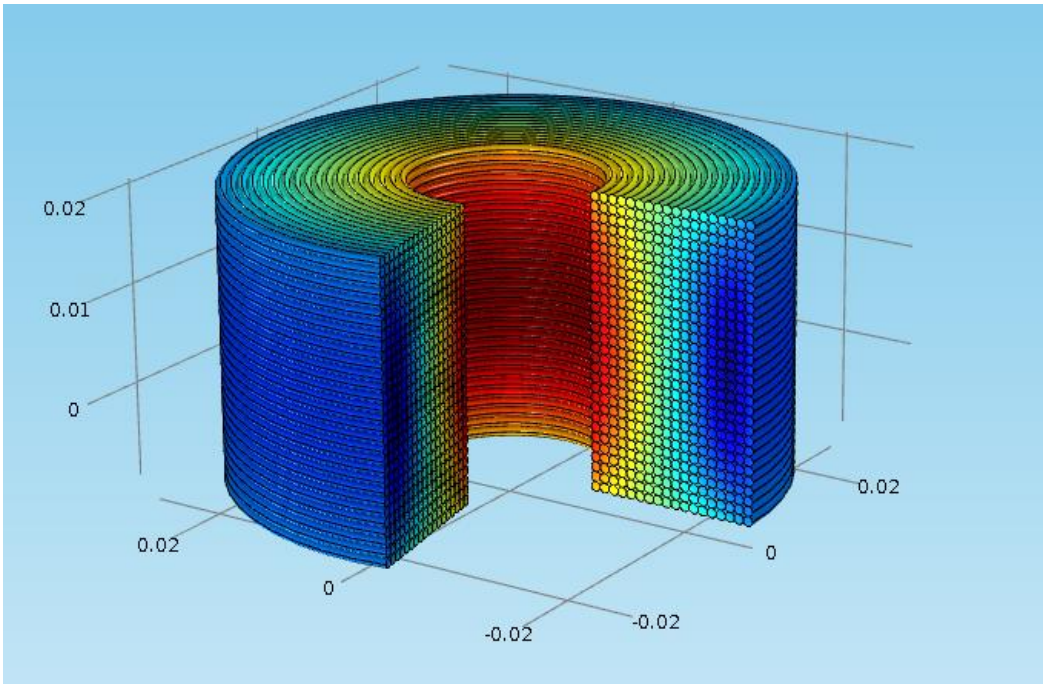

Figure 31:3D schematic of multi-layer coil

The cable diameter is 1mm, and there is no spacing between the cables. The generated magnetic field is shown in Figure 32:

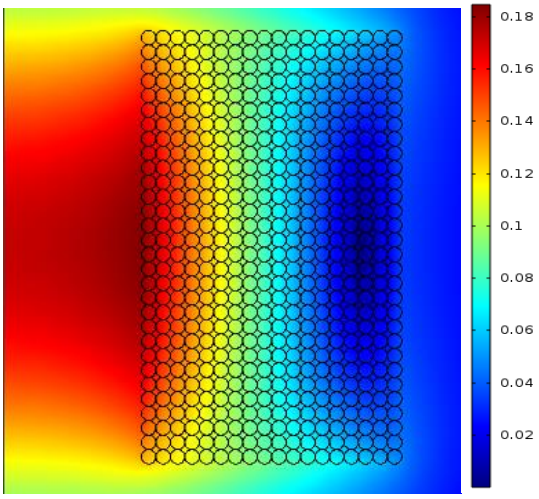

Figure 32: Colourmap of the magnetic field generated by the coil

In order to house the chiral pinene gas, we used a glass cell, with an isolated compartment, in which liquid pinene was placed. By submerging this compartment in salt-ice cooling baths, we were able to control the vapour pressure. Between the aforementioned compartment and the gas chamber itself, we placed a Thermovac so as to be able to measure the gas pressure at any moment. The chamber is sealed by using two high reflectivity AR coated windows. In the following figures, we can see a photo and a schematic of this glass cell.

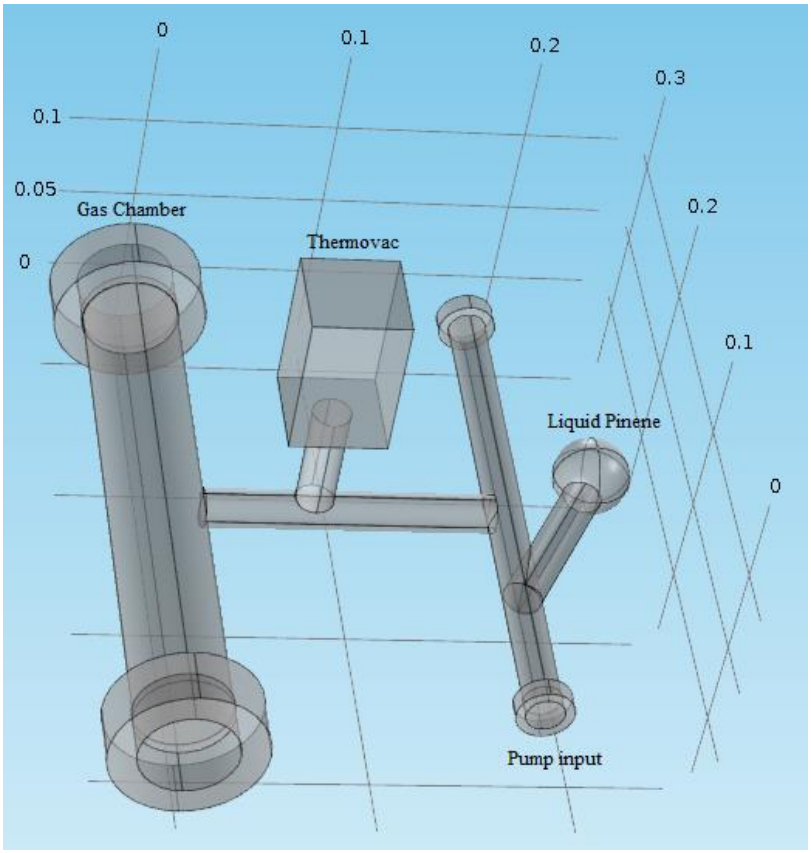

Figure 33: Gas cell schematic

Figure 34: Photo of Gas Cell

3.3 Process of measurement

We operate our 532 nm pulsed laser at a repetition rate of 10kHz and duty cycle of 99%. The signal was recorded through the use of a PC, equipped with a data acquisition card that supported 3 inputs. One is the trigger and the other two, were used to separately record the signals from the two counterpropagating beams.

The data acquisition process was performed by the Ultrachiral software which was developed by Photek, specifically for the aforementioned data acquisition card. The software GUI is presented in the following figure:

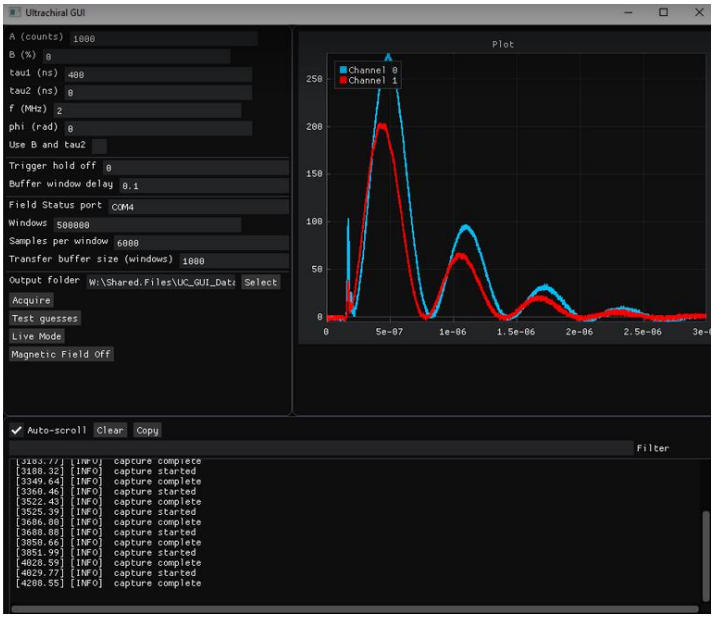

Figure 35: GUI interface

We observe numerous fields with numerical inputs. We proceed to explain what the fields of consequence represent:

Transfer Buffer Size (TBS): The number of pulses recorded and averaged, before giving the command to the relay, to switch the current direction and thus the magnetic field direction. The total number of pulses required to perform one complete measurement is 2xTBS

Windows: The total number of pulses recorded. This is used in order to perform multiple consecutive measurements.

Samples per window: Number directly proportional to the number of μs during which the ringdown of each pulse will be recorded.

Buffer Window Delay (BWD): The time during which no recording will be performed after current reversal. This is done in order to let the magnetic field settle to its stationary value.

Cut Points: The number of initial points removed from the recorded signal.

The rest of the parameters are used as initial guesses for the fitting module of the software. This module has not yet been put in use. Finally the software supports a Live Mode which displays the signal at any given moment.

The time needed for a complete measurement, with the parameters typically used is:

$$\tau_{meas} = 2\frac{TBS}{Repetition\ Rate} + BWD + Software\ Delays \approx 0.4 - 0.5s \quad (3.3.1)$$

The measurement time which we will henceforth refer to, is the setup specific time i.e., since the other contributions are due to outside factors which will in the future be removed.

$$\tau_{meas} = 2\frac{TBS}{Repetition\ Rate} = 0.2s \quad (3.3.2)$$

Finally in order to avoid any thermal effects, we start measurement once ~20 minutes have elapsed, after switching on the power supply.

3.4 Experimental Results

We start off by presenting results for consecutive measurements with an empty cavity, i.e. we have removed the gas cell itself and kept only the CeF_3 crystal.

First, we present the signals for two counterpropagating beams, under both magnetic field directions and the corresponding fits performed on them. These signals are produced by averaging the signals of 1000 consecutive pulses. The signals are denoted as CW^+, CW^-, CCW^+, CCW^-. The exponents refer to the direction of the magnetic field, whereas the bases refer to the clockwise and counterclockwise beams inside the cavity.

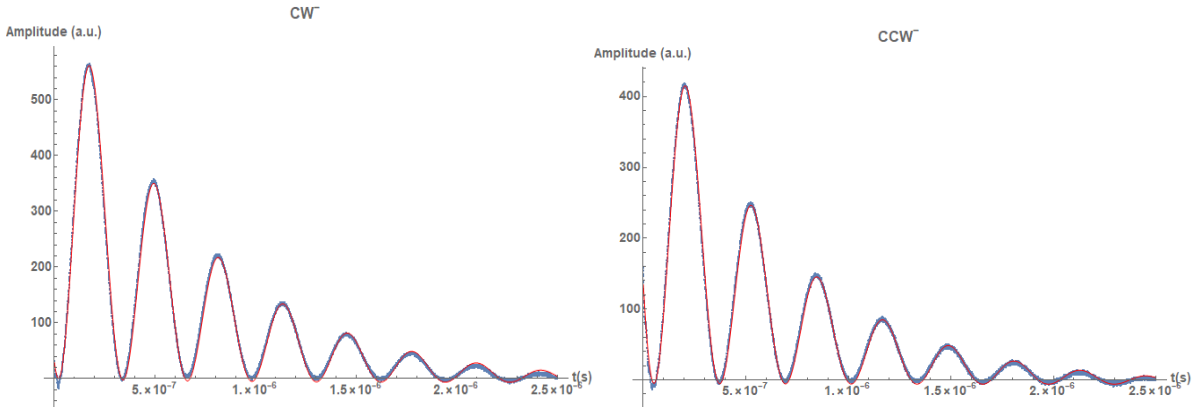

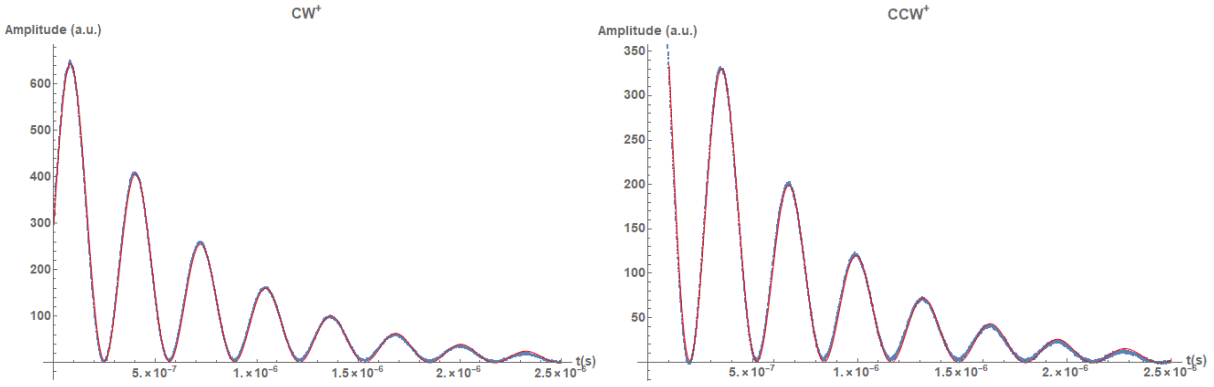

Figure 36: Individual signals and corresponding fits

We repeat the same process 250 times in order to determine the levels of noise and observe if there are any drifts or trends in the beating frequencies. The results are presented in the following figure:

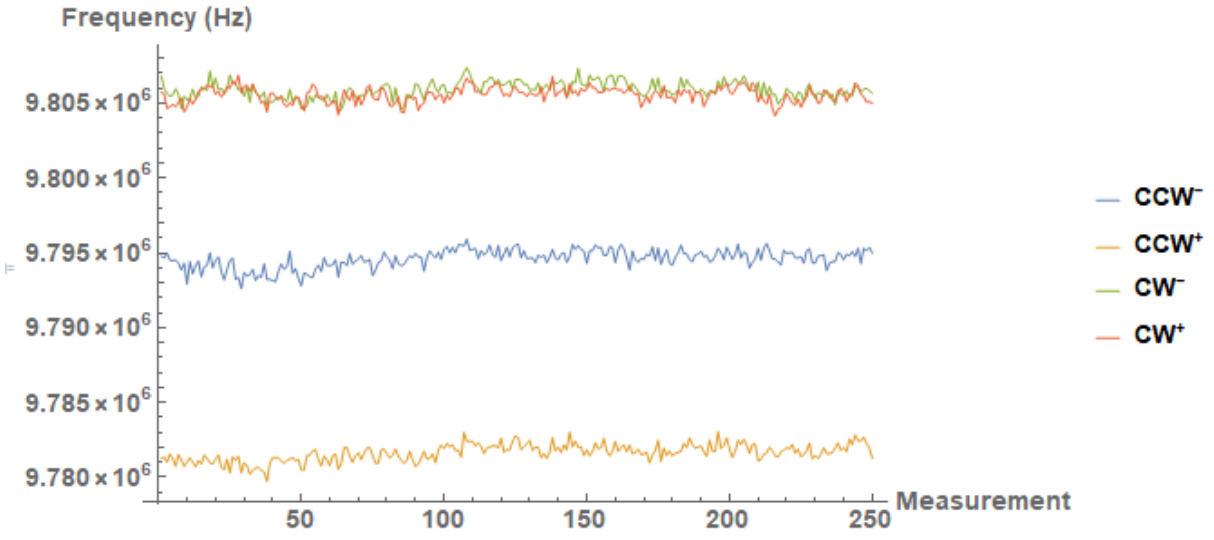

Figure 37: Frequencies of consecutive measurements

We observe that the frequency trend is repeated in all four signals, and thus is removed due to the two subtractions (due to magnetic field reversal and counterpopagating beams). Finally we derive the chiral angle itself.

The chiral angle results from the formula 2.5.3, using the frequencies derived from the 4 fits performed on the data, whereas the mean sensitivity is the standard deviation of the number of consecutive measurements made in one second, and represents the chiral angle error $\delta\varphi$ of a one-second measurement. The error improves proportionally to the inverse square root of measurement time as per:

$$\delta\varphi = \frac{Standard\ Deviation\ of\ measurements}{\sqrt{\#of\ measurements}} = \frac{\sigma}{\sqrt{\Delta t / \tau_{meas}}}$$

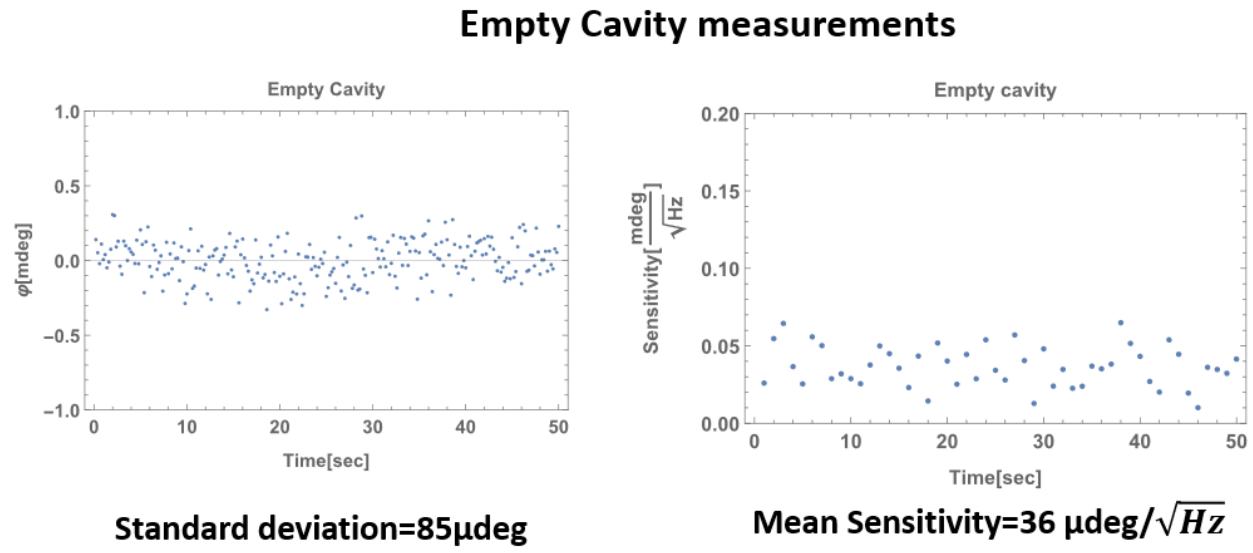

Figure 38: 50 consecutive one-second chiral angle measurements and the corresponding sensitivity

We then introduce the gas cell inside the cavity. This results in a drop in ringdown time due to light losses from the cell windows, which leads to reduced sensitivity. By submerging the compartment containing liquid pinene, into a slush bath, and slowly letting it thermalize, we can measure the chiral rotations at various pressures. The pressure is tracked by the Thermovac attached to the cell. After each measurement we pump the cell in order to re-measure the vacuum so as to be subtract any potential drifts.

The results are presented in the following figure:

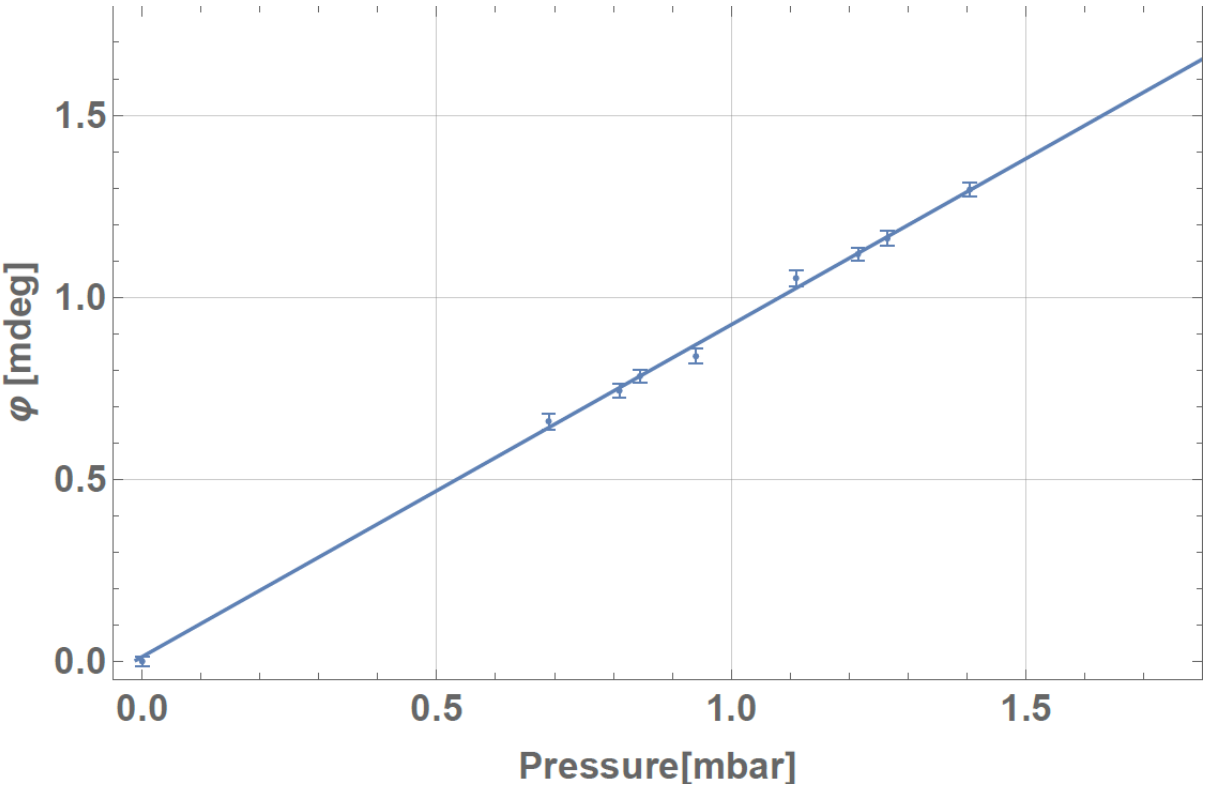

Figure 39: Pinene chiral rotations vs pressure

The slope is a_p=0.912 $\frac{mdeg}{mbar}$ which when converted to the usual units for optical activity yields:

$$a = 59.54 \pm 1.8 \frac{deg}{dm\ gr/ml}$$

Which is in excellent agreement with the interpolated value for 532nm from the Vaccaro measurements. Even more importantly, this value was determined, using angles that vary between them just a few tens of microdegrees. More specifically the error bar in each measurement is $\sigma = 10 - 20 \mu deg$

The individual frequencies measured from the 4 signals during the measurement process for a random angle were:

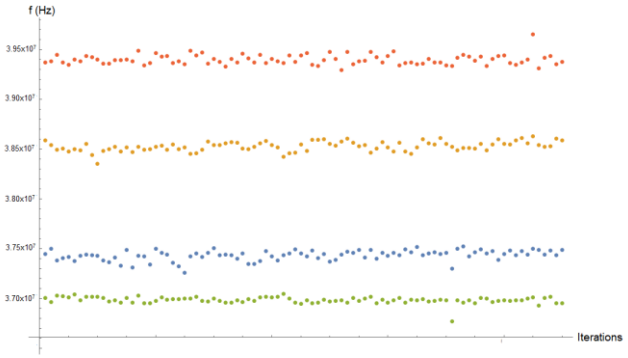

Figure 40: Measured frequencies

We thus observe, that the noise was minimal and no drifts were present.

Having established the fact that we can measure angles on the order of a few tens of microdegrees, we proceed to measure even smaller angles. We use an enantiomeric mix a-(+)-pinene and a-(-)-pinene with the first making up approximately 70% of the mix and the latter 30%. We performed consecutive measurement of vacuum and pinene, with a pressure difference of ~2.9mbar. The results are:

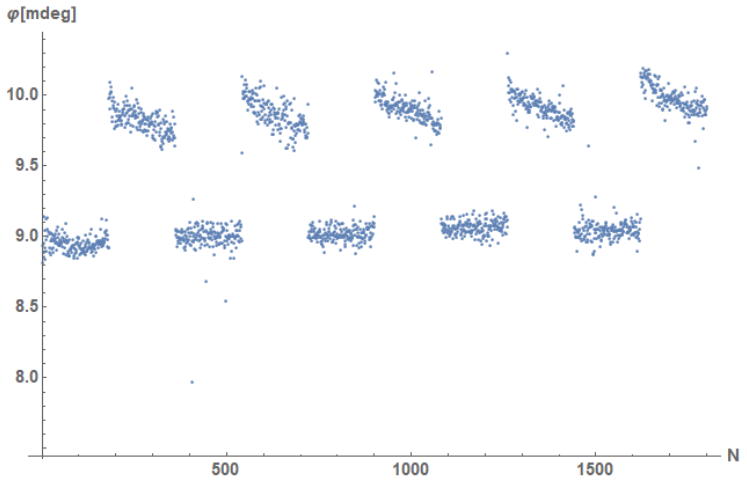

Figure 41: Consecutive angle measurements for 70-30 mix

By taking the mean and subtracting the two sets of values we get:

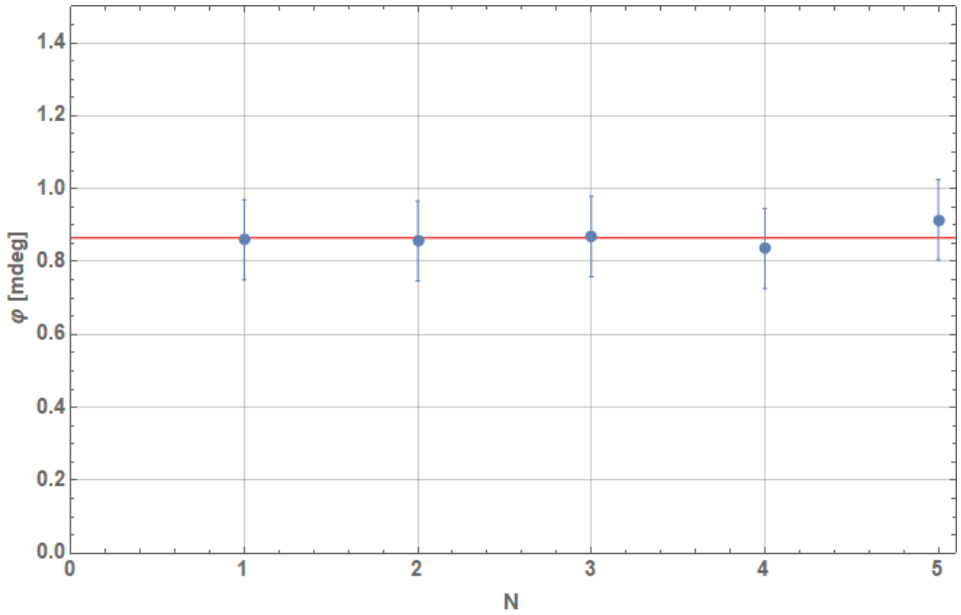

Figure 42: Mean angles measured for 70-30 mix

The angle measured was $\varphi = 0.86 \pm 0.11\, mdeg$, where the main source of error is our uncertainty in the enantiomeric mix percentages. The expected value according to our previously measured optical rotation, for a 70-30 mix was $\varphi_{exp} = 1.05 \pm 0.01 mdeg$. The two values are in good agreement, but a more accurate mixing process should be developed in order the further check our accuracy.

Furthermore a drift is present in the filled gas cell values, which is potentially due to the fact, that we did not wait long enough for the pressure to become fully homogeneous inside the cell.

In the future we plan to test our setup on more samples.

3.5 Miniaturization

We have already established the fact, that our setup provides unparalleled accuracy in optical rotation measurements. Modern market polarimeters have sensitivies approximately equal to $5\frac{mdeg}{\sqrt{Hz}}$ which is roughly 100 times worse than the one we presented. In order to make this setup marketable, it has to shrink to a more practical size.

This presents some difficulties. First and foremost, if we are to use a shorter cavity, the pulse width must also be reduced in order to avoid the pulse overlapping with itself. A good rule of thumb is:

$$\tau_{rt} \gtrsim 2\, FWHM \quad (3.5.1)$$

Furthermore, if we are to reduce the cavity size, great care must be taken to the dimensions of objects placed inside the cavity, so as to avoid overlapping with the beam path. This makes it nigh impossible to use a strong enough coil to generate a meaningful Faraday rotation, due to the fact that the cooling system is bulky and impractical. Yet another problem, is that we have to reduce the gas cell size, which leads to a reduction of chiral rotation per pass.

Considering these problems, we have proceeded to build a similar setup, to the one presented in chapter 3.1, with a few tweaks. The miniaturized cavity has arm lengths $L_1 = 27cm, L_2 = 7.5cm$ netting a round trip path of $L = 1.1m$ and a round trip time of $\tau_{rt} = 3.67ns$. The cavity is presented in Figure 43.

In order to avoid pulse self-coherence we have used a Microchip Laser, the pulse of which has $FWHM = 1ns$, and thus satisfies the condition 3.5.1. The main drawback is the reduced laser intensity which comes at the cost of accuracy and the slow repetition rate (1kHz) which increases the measurement time to:

$$\tau_{meas} = 2s \quad (3.5.2)$$

In order to be able to achieve a significant magnetic field, we have shifted paradigm, having abandoned the coil with the reversible current. Instead, we have used an array of permanent neodymium magnets, which are displaced relative to the magneto-optic crystal. The magnets have the shape of a hollow cylinder, so as to allow the beam to propagate through them. The field reversal is achieved mechanically, through and PC-controlled rotator coupled to the array. Whenever we want to reverse the field direction we just have to give the command to rotate the array by 360º. The main drawback is that this process requires significantly more time, on the order of a couple of seconds. The array we have used is presented in Figure 44:

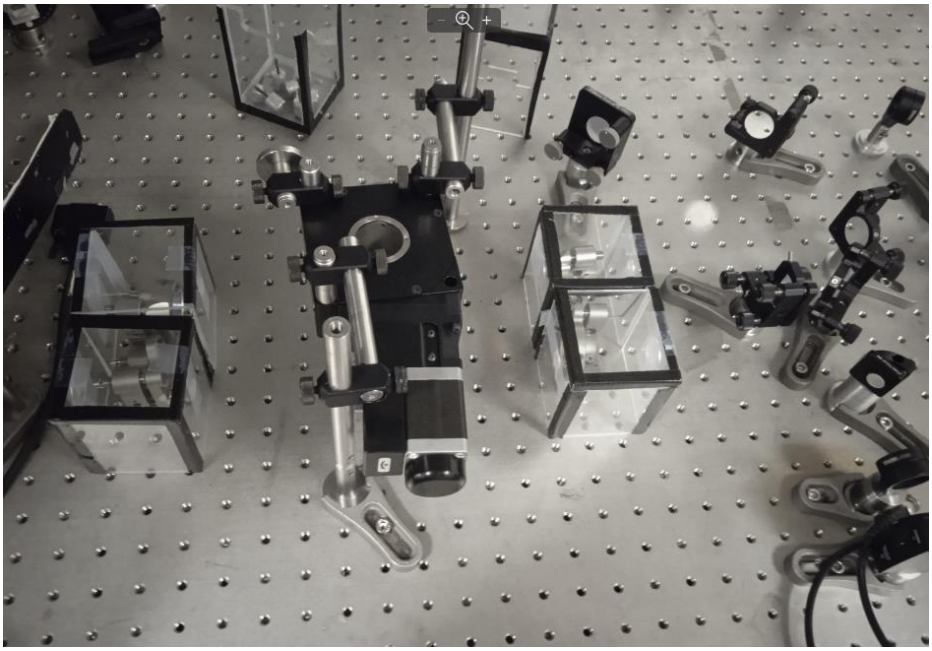

Figure 43: Miniaturized cavity photo

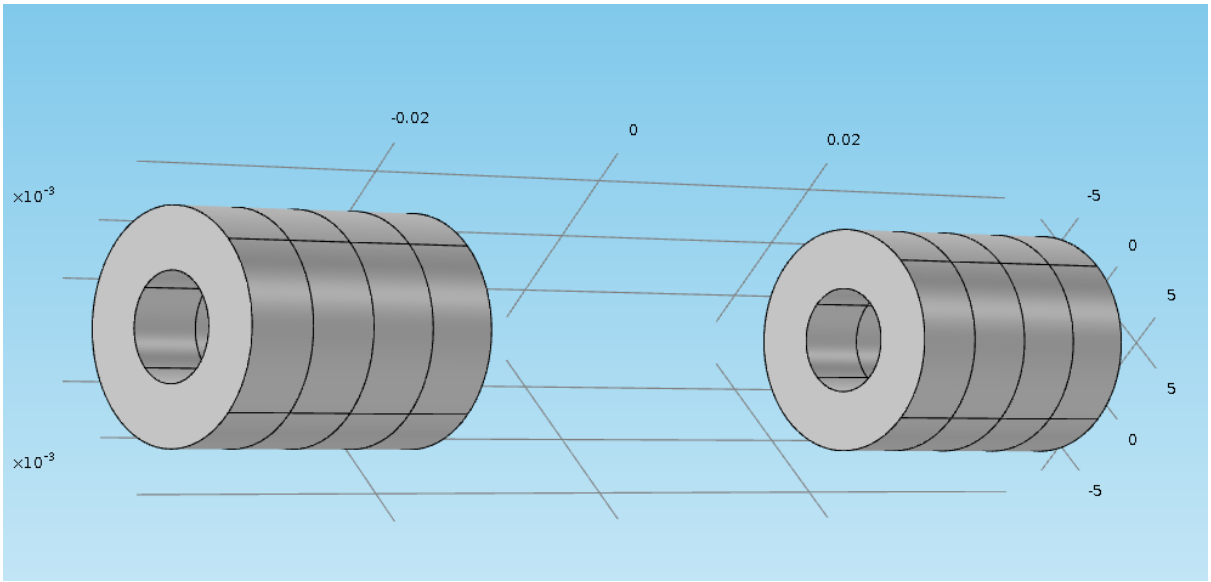

Figure 44: Permanent magnet array

The magnetic field generated in the space between the magnets is mostly co-linear to the beam propagation direction and is presented in Figure 45:

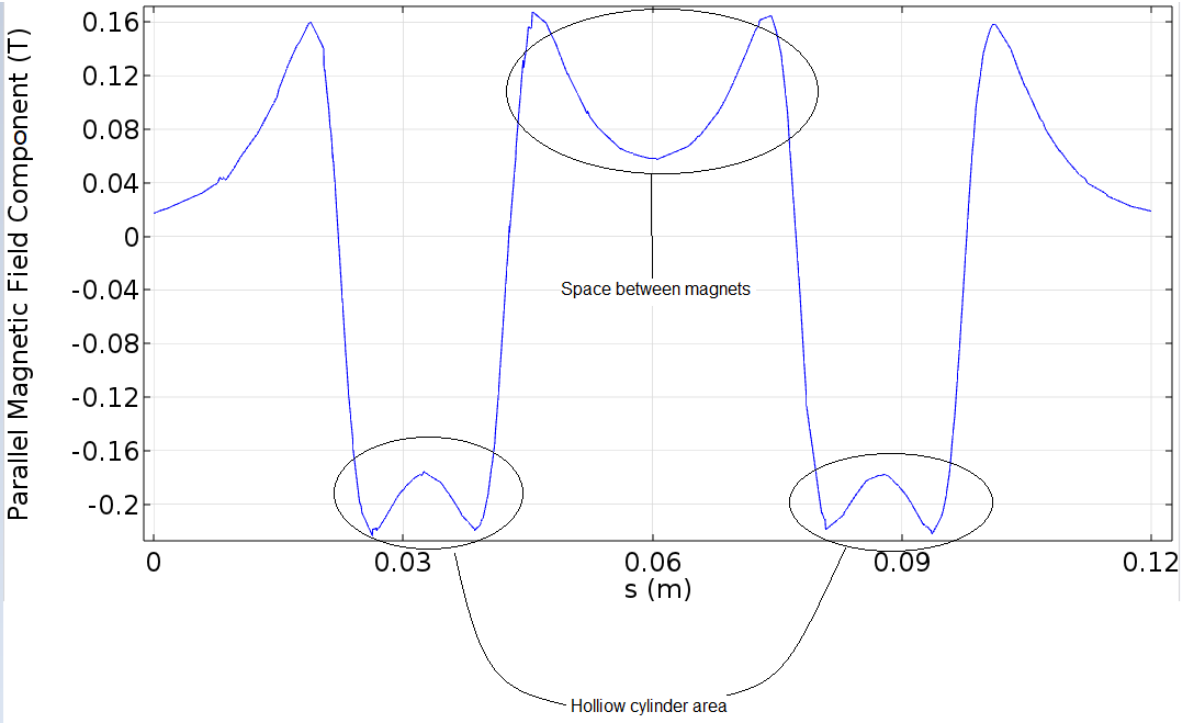

Figure 45: Magnetic Field generated by a neodymium array

We have not had the chance yet to run a full course of measurements in the miniaturized cavity, but we have tested the accuracy for the empty cavity. The results are presented in Figure 46:

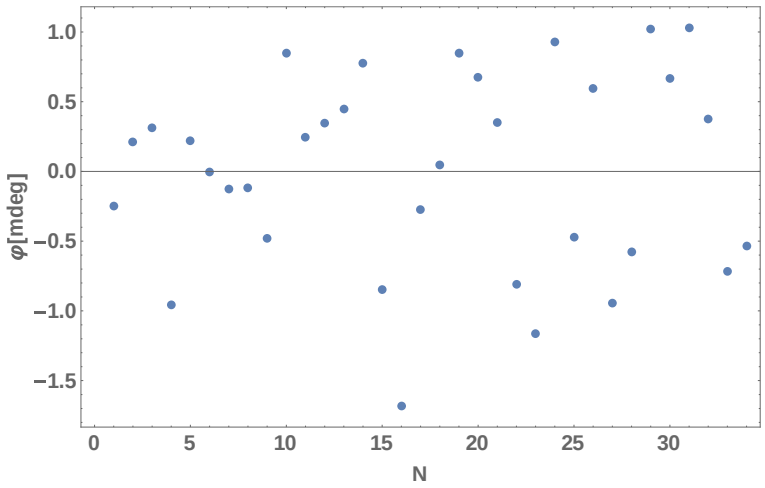

Figure 46: Miniaturized empty cavity results

The sensitivity is ~1 $\frac{mdeg}{\sqrt{Hz}}$, significantly worse than our previous sensitivity, but still multiple times better than that of market polarimeters.

3.6 Final Remarks

We have demonstrated a novel cavity based polarimeter setup, which exhibits unparalleled accuracy. We have presented results of measurements of gas phase samples, which produce minimal chiral optical rotations that are nigh undetectable through conventional methods. It is important to note the fact that this setup is not restricted to samples in the gas phase, but we have also in the past measured liquids with similar results. In the future we plan to attempt to measure thin dielectric films, once we have managed to consistently create such films with homogeneous enough surfaces.

In the future we also plan to make significant improvements such as:

- Employment of better optics
- New CeF_3 crystal with better coating
- GUI quality of life improvements
- Laser with shorter pulses and higher repetition rate and power
- Quicker and more practical scheme of magnetic reversal
- New coil with larger magnetic field
- Isolated cavity

These improvements will provide us with even better accuracy and faster measurements and at the same time increase the stability of our setup reducing the need for occasional realignments minimizing drifts and noises

Acknowledgments

I would like to thank the following people that made this work possible and whose help I vastly appreciate

First and foremost I would like to thank my supervisor Prof T.P. Rakitzis for being having introduced me to multiple fields and concepts in physics through his academic tutoring and for giving me a chance to work with his team. I would also like to thank him for always being ready and willing to help and the interest he has taken to me over the last few years.

Next up, I would like to thank Dr. George Katsoprinakis and Dr. Alexandros K. Spiliotis for always being willing to offer their help and knowledge and advising me over the years.

I would like to thank M. Xygkis and M. Koutrakis, who worked on the same experiment, making this thesis possible.

Finally I would like to thank again all the previous people and also E. Toutoudaki, Z. Sargianni, A. Linaraki for providing an excellent, fun and family-like work environment which made all this possible

References

1. Verdeyen, J. (1995). *Laser Electronics* (3rd ed.). Pearson.
2. Demtröder, W. (2014). *Laser Spectroscopy 1: Basic Principles* (5th ed. 2014 ed.). Springer.
3. Demtröder, W. (2015). *Laser Spectroscopy 2: Experimental Techniques* (5th ed. 2015 ed.). Springer.
4. Pedrotti, F. L., & Pedrotti, L. S. (1993). *Introduction to Optics (2nd Edition)* (2nd ed.). Prentice Hall College Div.
5. Polavarapu, P. L. (2018). *Chiral Analysis: Advances in Spectroscopy, Chromatography and Emerging Methods* (2nd ed.). Elsevier Science.
6. Lahiri, P., Wiberg, K. B., & Vaccaro, P. H. (2013). Intrinsic Optical Activity and Conformational Flexibility: The Role of Size-Dependent Ring Morphology in Model Cycloketones. *The Journal of Physical Chemistry A*, *117*(47), 12382–12400. https://doi.org/10.1021/jp4089194
7. Wiberg, K. B., Wang, Y. G., Murphy, M. J., & Vaccaro, P. H. (2004). Temperature Dependence of Optical Rotation: α-Pinene, β-Pinene Pinane, Camphene, Camphor and Fenchone. *The Journal of Physical Chemistry A*, *108*(26), 5559–5563. https://doi.org/10.1021/jp040085g
8. Kimball, D. F. (2001b). Progress towards fundamental symmetry tests with nonlinear optical rotation. *AIP Conference Proceedings*. https://doi.org/10.1063/1.1426796
9. Sofikitis, D., Bougas, L., Katsoprinakis, G. E., Spiliotis, A. K., Loppinet, B., & Rakitzis, T. P. (2014). Evanescent-wave and ambient chiral sensing by signal-reversing cavity ringdown polarimetry. *Nature*, *514*(7520), 76–79. https://doi.org/10.1038/nature13680
10. Bougas, L., Sofikitis, D., Katsoprinakis, G. E., Spiliotis, A. K., Tzallas, P., Loppinet, B., & Rakitzis, T. P. (2015). Chiral cavity ring down polarimetry: Chirality and magnetometry measurements using signal reversals. *The Journal of Chemical Physics*, *143*(10), 104202. https://doi.org/10.1063/1.4930109
11. Spiliotis, A. K., Xygkis, M., Klironomou, E., Kardamaki, E., Boulogiannis, G. K., Katsoprinakis, G. E., Sofikitis, D., & Rakitzis, T. P. (2020). Gas-phase optical activity measurements using a compact cavity ringdown polarimeter. *Laser Physics*, *30*(7), 075602. https://doi.org/10.1088/1555-6611/ab8d2e
12. Paschotta, R. (2021, July 17). *Cavities*. 2022 RP Photonics AG. https://www.rp-photonics.com/cavities.html

13. Paschotta, R. (2021b, November 28). *Gaussian Beams*. 2022 RP Photonics AG. https://www.rp-photonics.com/gaussian_beams.html
14. *Faraday Effect*. (n.d.). Fosco Connect. https://www.fiberoptics4sale.com/blogs/wave-optics/99205446-faraday-effect
15. Toutoudaki, E. (2021). *Cavity-enhanced atomic Iodine spectroscopy: Towards PNC optical rotation measurements* [Master's Thesis, University of Crete]
16. Generalic, E. F. O. C. A. T. (n.d.). *Chemistry Glossary: Search results for "chiral molecule."* Copyright © 2004–2020 Eni Generalic, All Rights Reserved. https://glossary.periodni.com/dictionary.php?en=chiral+molecule
17. *The Weak Interaction*. (2016). Warwick.Ac.Uk. https://warwick.ac.uk/fac/sci/physics/staff/academic/boyd/warwick_week/neutrino_physics/weak.pdf